TESI DI DOTTORATO

UNIVERSITA' DEGLI STUDI DI NAPOLI FEDERICO II

DIPARTIMENTO DI INGEGNERIA BIOMEDICA, ELETTRONICA
E DELLE TELECOMUNICAZIONI

DOTTORATO DI RICERCA IN
INGEGNERIA ELETTRONICA E DELLE TELECOMUNICAZIONI

Methods and algorithms
for electromagnetic waves propagation
in indoor environments

LUCA MURO

Il Coordinatore del Corso
Ch.mo Prof. Giovanni Poggi

Il Tutore
Ch.mo Prof. Giorgio Franceschetti

Anno accademico 2007–2008

Index

Introduction

The ability to provide reliable services, in wireless communication systems, is related to the characteristics (geometric and electromagnetic) of the propagation physical medium. In this context, the radio-coverage prediction is still a topic of great interest, both in the scientific community and among technology users. This interest produced a great number of electromagnetic propagation models, from which several computing algorithms have been developed, each one fit to a different application environment.

From surveys conducted among mobile operators, telecommunications networks installers and public institutions, come out that in general, the criteria for design and implementation of wireless networks, in indoor environments, are not rigorous, but based on some approssimative assumptions. From this grew the idea of developing academic research, aimed at streamlining the problem by building models, to be used as basis for prediction tools synthesis, fast and reliable both in terms of coverage efficiency, and of Protection from electromagnetic emissions.

The research topic in this thesis addressed concerns the development and subsequent validation of a method for analyzing the propagation of high frequency electromagnetic fields in indoor environments.

A first phase is focused on the main theory that describes the phenomena related to propagation at high frequency, in general and, in particular, for indoor environments (Chapter 1). The argument has been treated by exposing what are the effects of the interaction with the environment objects, both in frequency domain and in time domain, and how we can describe them with the mathematical tools available.

In a second phase we passed to analyze the possible models to adequately represent the propagation phenomena at high frequencies in indoor environments (Chapter 2), analyzing advantages and limitations of existing ones, and establishing an innovative method to study the problem. For developing a propagation model has been chosen to use Geometric Optics asymptotic solutions, that make it

possible to treat fields propagation phenomena by carrying out a decomposition in elementary contributions, easily calculable, and then assess the overall contribution by a elementary solutions superposition (via an incoherent sum). The environment model is based on various simplifications, dependent on assumptions related to the particular application here considered.

Subsequently, on the basis of the choices made in terms of models, has been designed and developed an algorithm, able to estimate distributions of electromagnetic field in indoors. The aim was to perform simulations, in order to compare them with measures. In this phase has been described the logic that governs the simulator modules, differentiating the different functions in terms of data input, data output and calculation algorithms, constituting the core of the system.

In the third phase (Chapter 3), once written a prototype of the simulator on the models defined, was first planned a series of simulations, in order to make an initial check on the results (in qualitative terms), defining canonical sources in canonical environments. An analysis carried out through simulations, in fact, was necessary for evaluating whether to introduce more complexity in the model of propagation; these checks corroborated some of the hypotheses from which derived our choices, taken during the modelization phase. Some modifications in the software have also been developed later, to perform an analysis in the time domain, calculating in all the points of the scene the mean delay and the RMS delay spread.

The final step was to validate the simulator through a comparison with quantitative measures.

For this purpose it was necessary to define a scene on which performing simulations and measurements, first identifying a real indoor environment and a real source, and then providing for them an appropriate characterization.

An ad hoc measurements protocol has been defined for this application. The methods for collecting, storing and processing measures, as well as the comparison procedures with the simulations, performed on the indoor scene model, are described in this part of the thesis.

Chapter 1

Theoretical introduction

The electromagnetic field general theory is able to solve general problems in any environment; in fact, having radiating source position and characteristics and having enough informations on surfaces discontinuities (boundary conditions), every problem on electromagnetic fields can be solved by means of Maxwell equations solutions.

This is a theoretical approach but, however, the reality is usually more complicated, due to the considerable difficulties introduced by the environment complexity, too hard to be described exhaustively. Because of these problems approximated methods were developed, that are simpler to be used in applications and, at least under certain conditions, are adequate to find solutions in some practical cases.

In this chapter some theoretical topics are investigated, that will be useful afterwards, in the next chapter, during the model definition for electromagnetic propagation in indoor environments.

1.1 Asymptotic solutions: Geometrical Optics

The *Geometrical Optics (G.O.)*, often referred to as *ray optics* (because it uses ray concepts), is an approach based on high-frequency approximations, in solving electromagnetic problems.

These approximations are used in the behaviour description of electromagnetic waves, when propagating towards obstacles of linear dimensions really greater than radiation wavelength.

Considering infinitesimal wavelengths (*lambda*) allows to study these waves, intercepting discontinuities of finite extension, as plane waves impinging on an undefined flat surface; in fact, when we consider

lambda tending to zero, small portions of spherical wave fronts can be locally represented as plane wave fronts, and in the same way any intercepted surface (depending on its local curvature radius) can be locally represented as a flat one.

To understand the propagation phenomena in these conditions it's necessary to analyze Maxwell equations in high frequency limits.

Consider a narrowband signal propagating in a linear, isotropic, lossless and time-invariant medium, with parameters $\varepsilon_0 \varepsilon_r$ and $\mu_0 \mu_r$, where relative permittivity and permeability ε_r and μ_r may be space-dependent.
In this case constitutive relationships are (in phasor notation):

$$\mathbf{D} = \varepsilon(\mathbf{r}, \omega)\mathbf{E}(\mathbf{r})$$
$$\mathbf{B} = \mu(\mathbf{r}, \omega)\mathbf{H}(\mathbf{r})$$

$$(1.1)$$

where the vectors $\mathbf{E}$ and $\mathbf{H}$ are complex functions depending on position, which determine magnitude and polarization characteristics of the field.
In regions where sources are absent the Maxwell equations can be written as:

$$\begin{cases} \nabla \times \mathbf{E}(\mathbf{r}) = -i\omega\mu\,\mathbf{H}(\mathbf{r}) \\ \nabla \times \mathbf{H}(\mathbf{r}) = i\omega\varepsilon\,\mathbf{E}(\mathbf{r}) \\ \nabla \cdot \varepsilon\mathbf{E}(\mathbf{r}) = 0 \\ \nabla \cdot \mu\mathbf{H}(\mathbf{r}) = 0 \end{cases}$$

$$(1.2)$$

If we define as free space *wavenumber* $k_0 = \omega\sqrt{\varepsilon_0\mu_0}$, $\zeta_0 = \sqrt{\mu_0/\varepsilon_0}$ as free space intrinsic impedance and $L(\mathbf{r})$ as the *eikonal function,* the total field associated to $\mathbf{r}$ can be written as follows:

$$\begin{cases} \mathbf{E}(\mathbf{r}) = e^{-ik_0 L(\mathbf{r})} \sum_{n=0}^{\infty} \mathbf{E}_n(\mathbf{r}) / (i\omega)^n \\ \mathbf{H}(\mathbf{r}) = e^{-ik_0 L(\mathbf{r})} \sum_{n=0}^{\infty} \mathbf{H}_n(\mathbf{r}) / (i\omega)^n \end{cases} \quad (1.3)$$

Substituting each of the previous expressions in the Maxwell equations, before mentioned, and using the well known formulas for curl and divergence computation, it results, in the high-frequency limit($\omega \to \infty$ and $k_0 \to \infty$):

$$\begin{cases} \nabla L \times \mathbf{E} = \mu \zeta_0 \mathbf{H} \\ \zeta_0 \mathbf{H} \times \nabla L = \varepsilon \mathbf{E} \\ \mathbf{E} \cdot \nabla L = 0 \\ \zeta_0 \mathbf{H} \cdot \nabla L = 0 \end{cases} \quad (1.4)$$

which constitute the *high-frequency limit* form of Maxwell equations.

In a lossless medium $\mathbf{E}$, $\mathbf{H}$ and L are to be considered as real quantities, and the equations (1.4) clearly show that $\mathbf{E}$, $\mathbf{H}$ and ∇L are mutually orthogonal, ∇L playing a role similar to the one played by the free space (vector) wavenumber $\mathbf{k}$, in the plane waves theory.

After a cross-multiplication (by ∇L) and a substitution, it can be found the following relationship:

$$\nabla L \times \mathbf{E} \times \nabla L = (\nabla L \cdot \nabla L)\mathbf{E} = |\nabla L|^2 \mathbf{E} = \varepsilon \mu \, \mathbf{E} = n^2 \mathbf{E} \quad (1.5)$$

that, ignoring the zero solution for $\mathbf{E}$, leads to the so called *eikonal equation*:

$$|\nabla L|^2 = n^2 \quad (1.6)$$

A system of curves that fills a portion of space so that, in general, a single curve passes through each point is a *congruence*. We can define the *ray vector* ∇L as: $\nabla L = |\nabla L| \hat{\mathbf{i}}$, where $\hat{\mathbf{i}}$ is the unit vector tangent to the beam propagation path; electromagnetic propagation in the high-frequency limit is described by the *ray congruence* $\nabla L = n\hat{\mathbf{i}}$ (obtained by using the equation (1.6) with the ray vector expression), orthogonal to the *rayfronts* $L(\mathbf{r})$=constant.
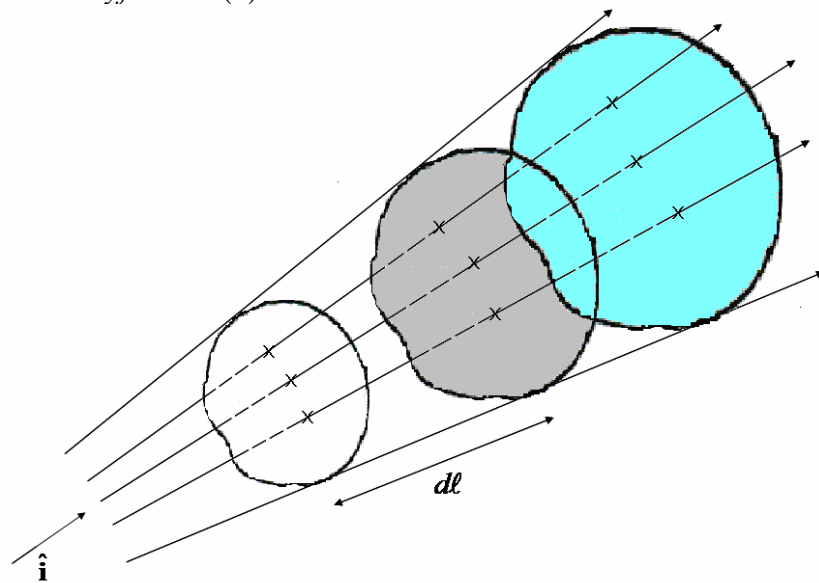

Figure 1.1 – A ray congruence and rayfronts associated.

A substitution in the first of the Maxwell equations (1.4) of the previous group leads to:

$$n\hat{\mathbf{i}} \times \mathbf{E} = \mu\zeta_0 \mathbf{H} \qquad (1.7)$$

So $\mathbf{E}$, $\mathbf{H}$ and $\hat{\mathbf{i}}$ are mutually orthogonal, too. This means that the field locally behaves as a plane wave propagating along the *ray path*.

These rays are generally not straight, as it could be thought, but it depends on the *eikonal equation* solution; in fact, to determine the

rays geometric configuration, it is necessary the refraction index $n(\mathbf{r})$ knowledge, in general varying from point to point in the space.

According to *Fermat's* principle, the shortest optical path between two points is that one along the actual *ray path* joining the two points; in an homogeneous medium, where the refraction index *n* is constant, the shortest optical path is the segment joining them.

If the $L(\mathbf{r})=0$ solution determines the initial *rayfront*, in general the value of $L(\mathbf{r})$ in another point $\boldsymbol{P}$ on the ray curve is equal to the optical path going from the first point (interception of the ray with the initial *rayfront*) towards the least. On this way, the field value corresponding to any wave front can be evaluated starting from its value on an initial wave front.

When the frequency tends to infinity, the Poynting vector expression is the following:

$$\mathbf{S} = \frac{1}{2\zeta}\left|E_0\right|^2 \cdot \hat{\mathbf{i}} \tag{1.8}$$

This means that the Poynting vector is along the ray directed, confirming again the previous results.

Consider a closed curve in the space and all the rays passing through it; all these rays define a surface constituting a pipe, and the enclosed volume represents a tube of rays.

Now if we take any couple of sections of this pipe, the *Poynting vector* flux ($dP = \mathbf{S} \cdot \hat{\mathbf{i}}\, dS$) is different from zero only through these 2 areas. In addition, the flux incoming from the first is the same of the one outgoing from the second. This happens for any equiphase surface in the tube of rays so, applying the classic energy balance on two of these surfaces (identified by their centres *O* and *P*), call them dS_0 and dS_1, we have:

$$dP_0 = dP_1 \Rightarrow \mathbf{S}(O)\cdot \hat{\mathbf{i}}\, dS_0 = \mathbf{S}(P)\cdot \hat{\mathbf{i}}\, dS_1 \tag{1.9}$$

and so:

$$\left|\mathbf{E}_0(P)\right| = \left|\mathbf{E}_0(O)\right| \cdot \sqrt{\frac{\rho_1 \cdot \rho_2}{(\rho_1 + \lambda) \cdot (\rho_2 + \lambda)}} \qquad (1.10)$$

where λ is the *distance-on-the-ray* between O and P, ρ_1 and ρ_2 are the radii of curvature of the dS_0 surface, and the dS_1 and dS_0 areas are approximated as rectangle flat surface areas, having the following analytical expressions.

$$dS_1 = d\theta_1 \cdot (\rho_1 + \lambda) \cdot d\theta_2 \cdot (\rho_2 + \lambda) \qquad (1.11a)$$
$$dS_0 = \rho_1 \cdot d\theta_1 \cdot \rho_2 \cdot d\theta_2 \qquad (1.11b)$$

To analyze some practical cases, we can suppose, for example, to have a point source, a linear source, or a plane wave. If we consider an electromagnetic field produced by a point source, in this case the radii of curvature become equal, and the wave front appears to be spherical; so, in formulas, we have $\rho_1 = \rho_2 = R$

and, consequently,

$$\left|\mathbf{E}_0(P)\right| = \left|\mathbf{E}_0(O)\right| \cdot \frac{R}{R + \lambda} \qquad (1.12)$$

whatever be the considered equiphase surface.

The λ parameter represents, again, the distance that exists from the point O to the point P. Now, if $\lambda \to \infty$, that is to say an observation point really far away from the source, the electromagnetic field goes to zero according to an $1/\lambda$ law, following the proportionality below reported.

$$\left|\mathbf{E_0}(P)\right| \propto \frac{R}{\lambda} \qquad (1.13)$$

In the second example, the source being linear (monodimensional), the wave front is represented by cylindrical surfaces. In this case, the ray of curvature ρ_2 goes to infinity and the analytical form for electromagnetic field, evaluated in the point P, is:

$$\left|\mathbf{E_0}(P)\right| = \left|\mathbf{E_0}(O)\right| \cdot \sqrt{\frac{\rho_1}{\rho_1 + \lambda}} \qquad (1.14)$$

going to zero following a $\sqrt{1/\lambda}$ law.

In the last example here proposed the wave front is no longer spherical or cylindrical, but a flat one: the radii of curvature are $\rho_1 = \rho_2 = \infty$, so we have, as relationship between the two fields values, the following:

$$\left|\mathbf{E_0}(P)\right| = \left|\mathbf{E_0}(O)\right| \qquad (1.15)$$

leaving a constant in module field, all along the *ray path*.

These are the rules for electromagnetic fields propagation into a homogeneous medium, in the high frequency approximation of the Maxwell equations. When impinging on a discontinuity, a ray behaves according to the *Snell*'s law; the reflected (and refracted, of course) field value can be evaluated knowing the Fresnel coefficients, the incoming field value and polarization.

This approach fails, for example, when there is a shadow zone behind obstacles (as wedges, edges, etc.), that cause a field discontinuity not physically justifiable; consider that it is an approximate model for frequencies going to infinite, that is to say interactions with objects very large, in terms of wavelength.
When these conditions happen no longer, the *Geometrical Optics* model goes into crisis and some correction strategies are necessary. This is the topic of the next paragraph.

1.2   Geometrical Theory of Diffraction

As we said before, the G.O. asymptotic solutions cannot be used correctly in some environments; this because only what happens on the ray is taken into consideration, in contrast with the general *waves theory*.

The Geometrical Optics is thus no longer applicable in every problem, because unable to fully explain the propagation phenomena in some environments. It's a matter of fact that, in a situation like that illustrated in the figure below, using only G.O. principles doesn't give us a correct solution in the shadow zone, where the field suddenly decays to zero. This happens because we don't take into account the diffraction.

The diffraction phenomenon occurs, for example, when a ray intercepts an half plane border, or an edge; the waves impinging on the edge begin to spread in directions not calculable with the *Geometrical Optics* formalism. This is the diffraction concept, formalized by Keller, among the others, in its *Geometrical Theory of Diffraction (G.T.D.)*; when these events occur we say that the electromagnetic wave is diffracted.
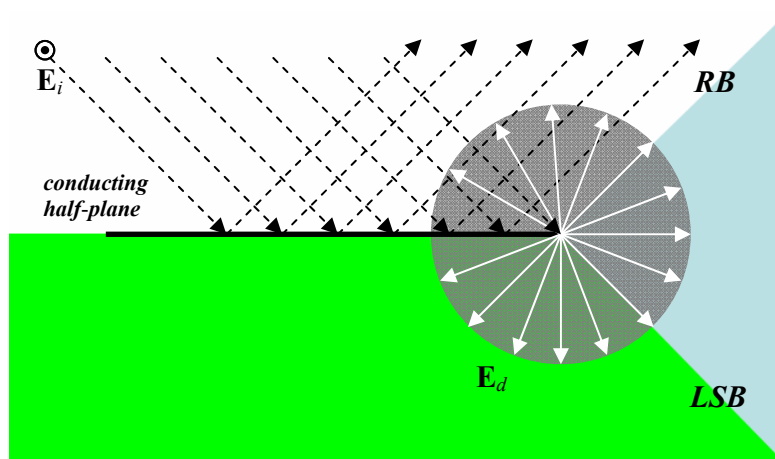

Figure 1.2 – Diffraction on a perfectly conducting half-plane edge.

Let's consider an example, with a perfectly conducting half-plane reached by a TE polarized plane wave

(the electric field being parallel to the edge; here it is called also *soft polarization*);the total electric field in a certain observation point P($\mathbf{r}$) in the space is the superposition of the incident electric field, of the field reflected by the half plane surface, calculated using the *Geometrical Optics,* and a third term that accounts for the diffracted field contribution.

As for the simple reflected or transmitted field, the diffracted field value is obtained by multiplying the incident field contribution value by a diffraction coefficient.

The exact solution to the problem leads us to the following expression, for the diffracted field by a perfectly conducting half-plane:

$$\mathbf{E}_d(\mathbf{r}) = - E_0 \frac{\exp[-i(\pi/4)]}{2\sqrt{2\pi k r}} \cdot$$
$$\cdot \left[\frac{1}{\cos((\varphi_j - \varphi_0)/2)} - \frac{1}{\cos((\varphi_j + \varphi_0)/2)} \right] e^{-i\mathbf{k}\cdot\mathbf{r}}\hat{\mathbf{i}}$$

(1.16)

where $\hat{\mathbf{i}}$ is the electric field unit vector, φ_j is the angle associated to the vector linking the edge to the observation point, and φ_0 is the wave incidence angle.

Obviously there is a formula describing $\mathbf{E}_d(\mathbf{r})$ for *hard polarization* [1] case, too; the only difference respect to the previous formula is a minus sign replaced with a plus sign, as reported below:

$$\mathbf{E}_d(\mathbf{r}) = - E_0 \frac{\exp[-i(\pi/4)]}{2\sqrt{2\pi k r}} \cdot$$
$$\cdot \left[\frac{1}{\cos((\varphi_j - \varphi_0)/2)} + \frac{1}{\cos((\varphi_j + \varphi_0)/2)} \right] e^{-i\mathbf{k}\cdot\mathbf{r}}\hat{\mathbf{u}}$$

(1.17)

---

[1] The magnetic field is parallel to the edge.

where $\hat{\mathbf{u}}$ is the electric field unit vector.

In case of oblique incidence the G.O. rules of reflection are used; the rays scattered by the edge are confined over a conical surface named *Keller's cone,* such that the incidence and reflection angles have the same value, call it β. The diffracted field is calculated by means of a matricial diffraction coefficient **D**, as described below:

$$\mathbf{E}_d(\mathbf{r}) = \sqrt{\frac{2}{\pi kr}}\, e^{-ikr}\, \mathbf{D}\cdot\mathbf{E}_0 \tag{1.18}$$

where

$$\mathbf{D} \longrightarrow \frac{1}{\sin\beta}\begin{vmatrix} D_\perp & \\ & D_\parallel \end{vmatrix} \tag{1.19}$$

is the *edge diffraction matrix,* $D_\parallel$ and $D_\perp$ being the scalar coefficients (*edge diffraction coefficients*) for *soft* and *hard polarization* formulas, with the following analytical form (+ for the *hard* case and - for the *soft* one):

$$D_{\perp\parallel} = -\frac{\exp[-i(\pi/4)]}{4}\left[\frac{1}{\cos((\varphi_j - \varphi_0)/2)} \pm \frac{1}{\cos((\varphi_j + \varphi_0)/2)}\right] \tag{1.20}$$

For each of the formulas for diffracted field evaluation, above illustrated, there is a relationship between **E** and **H** ($\hat{\mathbf{i}}$ being the Poynting unit vector):

$$\zeta\mathbf{H}_d = \hat{\mathbf{i}}\times\mathbf{E}_d . \tag{1.21}$$

When the material constituting the half plane surface is no longer conductive, but is a dielectric, appropriate Fresnel coefficients (depending on polarization) appear in the *edge diffraction coefficients*:

$$D_{\perp\|} = -\frac{\exp[-i(\pi/4)]}{4}\left[\frac{1}{\cos((\varphi_j - \varphi_0)/2)} + \Gamma_{\perp\|}\frac{1}{\cos((\varphi_j + \varphi_0)/2)}\right] \quad (1.22)$$

There is a limit in the GTD approach, due to the field diverging at the *reflection boundary* (RB) and at the *lit-shadow boundary* (LSB), where $\varphi_j \longrightarrow \pi \pm \varphi_0$.

To overcome this limit it is necessary to use some corrections, as it has been done here (see chapter 3), or in the *Uniform theory of Diffraction* (UTD), for example.

1.3   Time domain analysis

In indoor environments signals are usually strongly subject to interference, so it is important, in a wireless communication system, to characterize the indoor radio channel in the best way possible.
In a typical indoor radio system there is a fixed transmitting antenna that communicates with more receiving terminals within the building, either portable or fixed.
Because of the radio waves reflection, scattering and diffraction phenomena, due to the presence of different structures inside, the transmitted signal reaches the receiver from more than one direction, giving rise to a phenomenon known under the name of *multipath fading*. The various signal components reach their destination through various paths, indirect or direct depending on source and destination positions; if in *line of sight* (LOS), typically there is a first (direct) contribution and then also some replicas, coming from other directions, after some interactions with environment surfaces. Obviously the replicas will come on the destination differently delayed and attenuated, depending on different paths followed. All these different components (coming in different times) will combine at the receiver, resulting in a distorted version of the transmitted signal. The phenomenon becomes more and more complicated when the transmitter and the receiver are in relative motion one respect to

each other; in this case there could be another signal alteration, due to the Doppler effect.

The electromagnetic propagation inside a building is subject to very complex multipath phenomena, much more than in outdoors, because of the environment, that is characterized by a strong confininement capacity on the electromagnetic waves spreading inside. Some differences in materials characteristics are significant too, passing from building to building; in a farm, for example, materials used for the structure construction are quite different, if compared to those used in offices buildings. The variability of the materials used in a building, the internal partitions, the perimetral walls facing outside, the ceilings and buildings floors themselves are important factors that influence the indoor electromagnetic propagation, such as the shape and the presence of windows, the structure age and so on.
These are the reasons because it is necessary to formalize these phenomena in general. In the next chapters, the time domain analysis will be detailed in the indoor environment.
In the next section are introduced the time dispersion, resulting from multipath in a generic environment, and also the frequency dispersion, due to a source that, for example, is moving towards its receiver.

1.3.1 Multipath fading

Assume fixed both the transmitter and the receiver position: we first want to understand the effect on the signal we receive.
First, let's consider a single Dirac pulse $x(t) = \delta(t)$ transmission and imagine to receive the signal only from two directions. This means that what you receive can be represented analytically as:

$$y(t) = x(t) + \alpha \cdot x(t - \tau) = \delta(t) + \alpha \cdot \delta(t - \tau) \qquad (1.23)$$

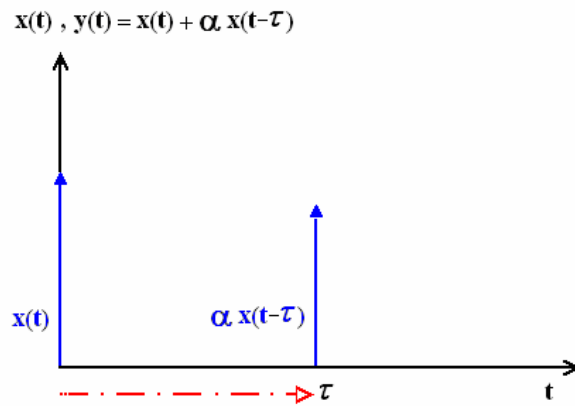where y(t) is normalized respect to the first contribution ($\delta(t)$) attenuation coefficient.

x(t) , y(t) = x(t) + α x(t-τ)

x(t)

α x(t-τ)

τ   t

Figure 1.3 - A delayed replica of a Dirac pulse.

What can be seen is that, at the receiver, it is found the presence of the transmitted pulse $x(t)=\delta(t)$, superposed to a delayed replica coming τ second later and reduced in amplitude by a factor α (see *Figure 1.3*). In this case, using an ideal pulse, it is easier to note that in reception the two received signals can be distinguished and then, instead of ignoring the replica, it could be used to extrapolate better information about the channel behaviour.

In real situations, in transmissions, ideal pulses are obviously never used, but signals are always characterized by a certain finite time duration T_x. In this case, more realistic, if it happens that the condition $T_x << \tau$ is met, it is anyway possible to distinguish the replicas arrived at the receiver. Usually the transmitted signal time duration T_x is inversely proportional to its bandwidth B_x, by it occupied; therefore the condition to be verified to distinguish replicas arrived at the receiver is $1/B_x << \tau$, that is to say $B_x >> 1/\tau$. When it happens that the sent signal bandwidth is very large, the replicas reaching the receiver can be distinguished, avoiding the fading problems due to multipath propagation [2].

---

[2] The hypothesis at the basis of this reasoning is that only one signal is transmitted, so there isn't another signal, transmitted τ seconds later, for example, that can be corrupted by the replica associated to the previous one.

Conversely, if we increase the transmitted signal duration, the signals coming in the same receiving point begin to overlap and, therefore, could not be identified as individual signals; the result would be an altered version of the initially transmitted signal.

It is interesting to analyze in detail what happens in these cases. Suppose, this time, a finite bandwidth signal *x(t)* (with a finite duration in the time domain, of course), and a replica, delayed of an amount of time equal to τ (see *Figure 1.4*), whose attenuation is represented by a coefficient α < 1;

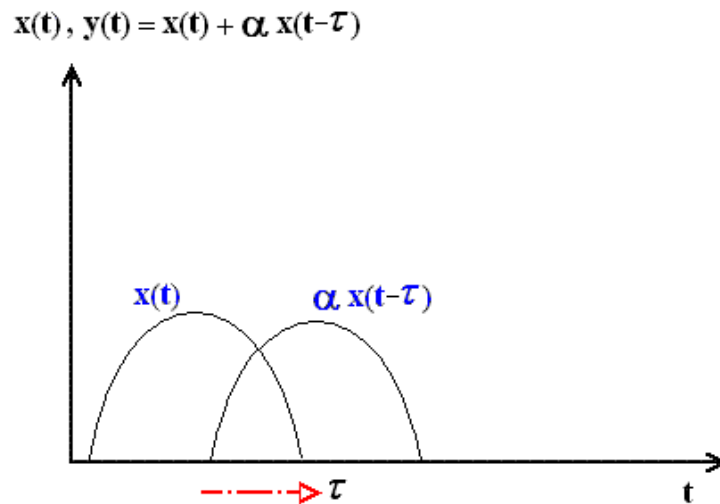**x(t) , y(t) = x(t) + α x(t-τ)**

Figure 1.4 - A delayed replica of a real pulse.

In a more general case, usually, there isn't only one replica reaching the destination point, but there is a greater number, depending on how many the possible paths are, along which the travelling signal is able to reach the receiver. In this case the analytical form of the (total) received signal is:

$$y(t) = \sum_n \alpha_n \cdot x(t - \tau_n) \qquad (1.23)$$

where $\alpha_0 \cdot x(t - \tau_0)$ is the first contribution coming, in LOS (line of sight) or NLOS (non-line of sight); as can be seen in the formula here we didn't use normalizations anymore.

It is intuitive that, if the various signals reaching the observation point came not hardly delayed [3] , one respect to each other, the replicas (and the transmitted signal, of course) overlap in reception almost perfectly; in this case we could have a multipath fading anyway, because the different replicas paths differ respect to the transmitted signal and one respect to each other, and consequently the associated temporal delays τ_n are different, too. This means that the different signals overlapping at the receiver should have different phase deviations, and their sum should result in a field value weaker than the free space one; in this situation the transmitted signal "sees" a channel almost flat, in its frequency band, and the effect is that each frequency component of the signal is attenuated of the same amount. When the only effect of the multipath propagation is a constant attenuation in the signal band, we call it *flat fading*.
When the signal bandwidth B_x is larger, the amount of fading by multipath propagation can vary from frequency to frequency, into the signal band; the "frequency selective fading" term expresses the correlation lack between the different components of the transmitted signal spectrum.

Obviously, not all the contributions have the same field amplitude: more are the events occurring along the replica path, like diffractions and reflections, less is the signal level associated. It is necessary to define parameters, for channel description, in which the different contributions delays are weighed with their signal amplitude.

Two parameters that take in account both the delays to the different contributions associated and their attenuation are the *mean delay T_0*, whose definition is:

$$T_0 = \sum_{n=1}^{N} A^2{}_n \, \tau_n \bigg/ \sum_{n=1}^{N} A^2{}_n \qquad (1.24)$$

---

[3] If very small, compared to the signal duration, the delay is considered negligible.

and the *delay spread*, that is a measure of the delays spreading around the mean value:

$$\sigma_\tau = \sqrt{\sum_{n=1}^{N} A^2{}_n \left(\tau_\mathrm{n} - T_0\right)^2 \Big/ \sum_{n=1}^{N} A^2{}_n} \qquad (1.25)$$

With these parameters we can define the condition under which the distortion can be considered negligible, as said before. If

$$\sigma_\tau << 1/B_x \qquad (1.26)$$

there is no frequency selective fading. If we define another parameter, the *coherence bandwidth*, as:

$$B_c = 1/\sigma_\tau \qquad (1.27)$$

the previous condition can be rewritten as follows.

$$B_c >> B_x \qquad (1.28)$$

The coherence bandwidth of a channel affected by multipath is, in conclusion, a measure of the frequency range in which the channel weighs all the transmitted signal spectral components with approximately equal amplitude; two frequencies of this amount far each other, in the signal spectrum, are the closest of those which the channel begins to treat differently. This means that if you get $B_c >> B_x$ the sent signal *x(t)* is not distorted by the channel, that does not show a selectivity in frequency.
Conversely, if $B_x \approx B_c$, the channel begins to treat frequency components differently.

Let's examine some examples of high-frequency signal transmission. Consider a GSM signal, first, characterized by a 200 kHz bandwidth, and a "spatial delay", between the signal and one replica, of 30.0 meters, the corresponding delay spread is, in seconds:

$$\sigma_\tau = \frac{30.0}{3 \cdot 10^8} = 10^{-7} \qquad (1.29)$$

In this case $\sigma_\tau = 2 \cdot 10^{-2} / B_x$, so the spread can be ignored.

If we consider, now, an UMTS signal, the bandwidth of 5 MHz requires greater attention. Even if the CDMA channel access method is intrinsically less vulnerable to the multipath fading, in this case the delay spread is $\sigma_\tau \approx 1/B_x$; for this reason, in this application, the delay spread will be taken into account (see chapter 3).

1.3.2 Doppler frequency spread

Let's examine, now, what happens when there is a relative motion between a transmitter and a receiver if, for example, a single frequency tone is transmitted; in the time domain it could be analytically represented by a simple expression like the following:

$$x(t) = e_0 cos(\ 2\pi f_0 t - \mathbf{k} \cdot \mathbf{r} + \varphi_0) \qquad (1.30)$$

where f_0 is the original transmission frequency, $\mathbf{k}$ is the (vector) wave number and $\mathbf{r}$ is the observation vector.

If $\boldsymbol{v}$ is the relative velocity[4] between a transmitter and a receiver, the observation vector can be written as a function of this velocity and time, and so the previous relationship becomes:

$$x(t) = e_0 cos(2\pi f_0 t - \mathbf{k} \cdot \mathbf{r}_0 - \mathbf{k} \cdot \mathbf{v}\, t + \varphi_0); \qquad (1.31)$$

this means that in the observation point is no longer received the same transmitted frequency f_0, but a new frequency, given by the difference f_0-f_D, where $f_D = (f_0/c)\hat{\mathbf{k}} \cdot \mathbf{v} = f_0(v/c)\cos\vartheta$ is a frequency translation,

---

[4] We consider, here, a uniform velocity.

proportional to both the transmitted signal carrier frequency f_0 and the dot product between **k** and **v**.

This frequency translation f_D is positive or negative depending on the relative motion of the receiver respect to the transmitter: if they approach each other, then $f_D < 0$; otherwise, f_D becomes positive.

The received signal is thus subject to a constant frequency translation.

If different paths exist, through which the transmission signal reaches the receiver (multipath propagation phenomenon), in this way a series of new frequencies f_n appears, which are all given by a different *Doppler shift*, representing the frequency translation of the single received contribution, function of the transmission frequency. Their expression is, depending on each different path, given by the same relationship as before:

$$f_{Dn} = f_0(v/c)\cos\vartheta_n \qquad (1.32)$$

As ϑ_n values change with n, so change the values of the frequencies received.

So if we consider both Doppler spread and multipath propagation phenomena and assume, for example, only two paths reaching the observation point (one of them being the direct LOS path), the relative motion between transmitter and the presence of a replica generate two signals, at the receiver, one at $f_1 \neq f_0$ frequency and another at $f_2 \neq f_0$ frequency (see *Figure 1.5*).

In this way we have a frequency dispersion. The Doppler effect causes a change in the form of transmission signal which corresponds to a distortion of its waveform. In this case we can argue that the channel begins to introduce a time selectivity.

The frequency dispersion means a signal bandwidth increasing: when a signal is under its influence, the channel changes its characteristics during the propagation of the signal itself.

Unlike the frequency selectivity, that describes an increase of the signal duration in time, because of a selectivity introduced in the frequency domain, the *Doppler frequency spread* describes an

increase of the signal occupation in frequency, because of a selectivity introduced in the time domain. In practice they are dual one respect to each other, representing two faces of the same problem.
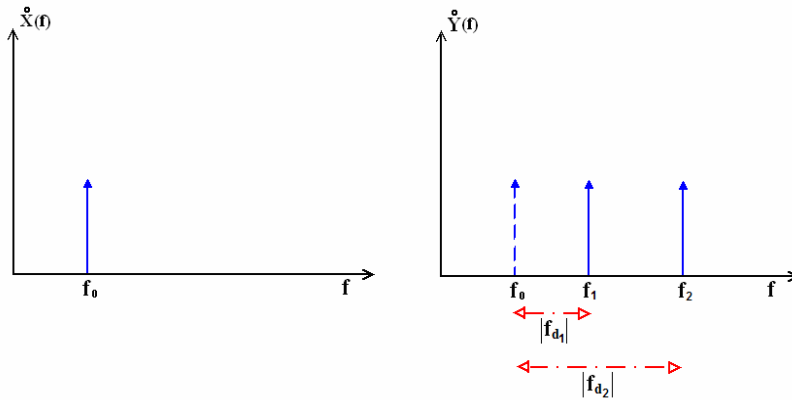

Figure 1.5 – Frequency spread.

Following this way of thinking, it's natural to define a parameter that, as the *delay spread* in time domain, describes this increase in the frequency one, too. This is the *Doppler spread* (*Bd*), defined as the maximum of the possible spectral dispersions, due to the time variance characterizing the channel under observation:

$$Bd = \max_{n} f_{dn} \qquad (1.33)$$

If existing a path with $\cos \vartheta_n = 1$, linking source and destination,

$$Bd = f_0(v/c). \qquad (1.34)$$

Following this way we can define another significant parameter, dual respect to the coherence bandwidth: the *coherence time T_c*:

$$T_c \approx \frac{1}{B_d}. \qquad (1.35)$$

Its value represents a measure of temporal variability of the channel; if the signal duration is much less than coherence time value, then there is no distortion, because the channel doesn't have time to change its behaviour. Conversely, if the signal duration is greater than coherence time value, the channel shows selectivity in time. A great Doppler spread involves a small coherence time, that is to say the under observation varies very quickly over time.

In the applications here considered, anyway, the relative velocity v is, as a matter of fact, very slow. This means that $v/c \ll 1$, in a indoor environment, and the Doppler frequency spread should be negligible; for this reason it will be, here, ignored.

So, how so far shown, it is clear that the transmitted signal characteristics, both temporal and frequencial, are of fundamental importance, once known the behaviour of the channel under observation, through which it must be propagated.

If we consider, then, a generic transmission, with symbols whose duration is T_x and total bandwidth is B_x, the conditions to be met to ensure a received signal without distortions are well explained in Figure 1.6.

On the two axis are represented time and frequency, with T_x being the signal duration and B_x being the signal bandwidth. Two values are fixed in this diagram: the coherence time T_c and the coherence bandwidth B_c; these are the thresholds over which the channel begins to behave as a selective one.

• If $B_x \ll B_c$, the transmitted signal bandwidth is much smaller than the coherence bandwidth, so there is no dispersion over time and the channel is considered flat in frequency, not introducing in this domain any selectivity; this means that over the channel all the signal spectral components are treated in the same way;

• If $T_x \ll T_c$, the transmitted signal duration is much smaller than the channel coherence time, so there is no dispersion in frequency and the channel is considered flat over time, not introducing any selectivity in

this domain; this means that the signal passing through the channel can't see any changes over time, because channel behaviour changes are significant only over a time period much greater than signal duration.
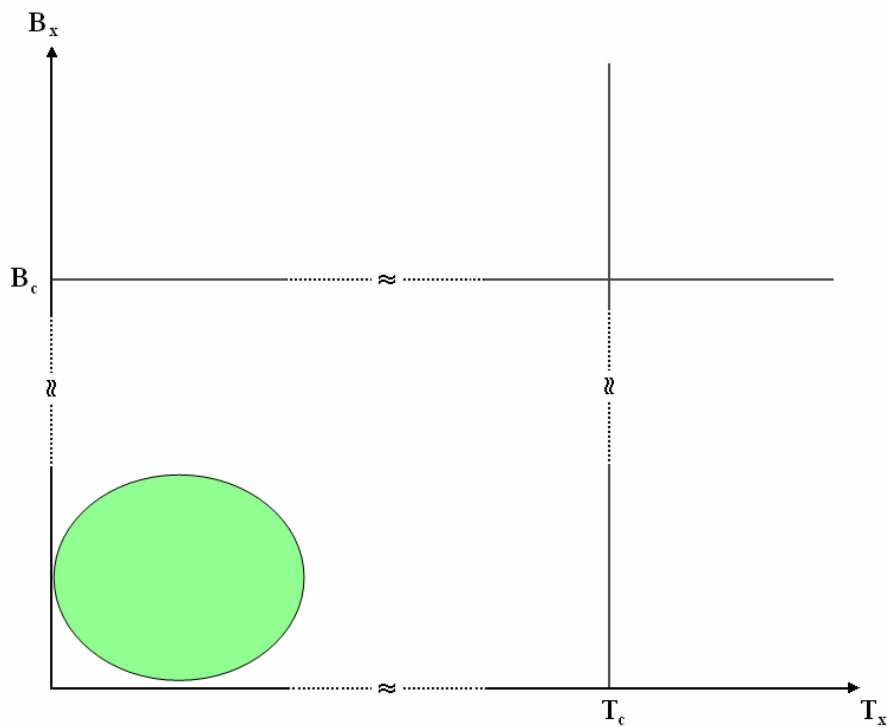

Figure 1.6 – Time-frequency dispersion diagram.

Obviously, if simultaneously satisfied both of the previous conditions (so we are in the green circle in figure 1.6), the channel model to be adopted is the most simple possible: flat in time and in frequency. In all the other situations the signal passing through the channel experiments some alterations, in frequency, in time or in both of them.

References

[1] Giorgio Franceschetti,"Electromagnetics Theory, Techniques, and Engineering Paradigms", Plenum Press, New York & London (1997);

[2] C. A. Balanis, "Advanced Engineering Electromagnetics", New York: Wiley (1989);

[3] Henry L. Bertoni, "Radio Propagation for Modern Wireless System", Prentice HALL PTR (2000);

[4] J. B. Keller, "Geometrical Theory of Diffraction", Journal of the optical society of America vol. 52, N2, 1962;

[5] S. Benedetto, E. Biglieri, V. Castellani, "Teoria della Trasmissione Numerica", Jackson Libri (1990);

Chapter 2

Model and algorithm definition

The scientific community has so far developed a wide range of electromagnetic propagation models, each particularly suited for specific applications. Starting from these models new algorithms can be implemented, really useful to analyze propagation phenomena in a certain environment. The dielectric properties of materials constituting objects (walls, doors, etc.) involved in wave propagation, for example, as well as the geometric model of the scenario, deeply affect the accuracy of electromagnetic field behaviour prediction. A basic problem to solve in analyzing the field propagation, therefore, is to describe the propagation environment, accurately and realistically as possible. In this chapter the choices made during the modelling operations are presented, in terms of propagation and environment description.

2.1   Models classification

A propagation model targeted for the indoor environment comes from a necessary compromise between the need for simplicity (so that, the model is practically usable) and the need to correctly and detail (enough) describe a scenario and the propagation mechanisms. A first useful simplification is to limit the propagation phenomenon, which by its nature is inherently three-dimensional, only on two reference geometric plans.
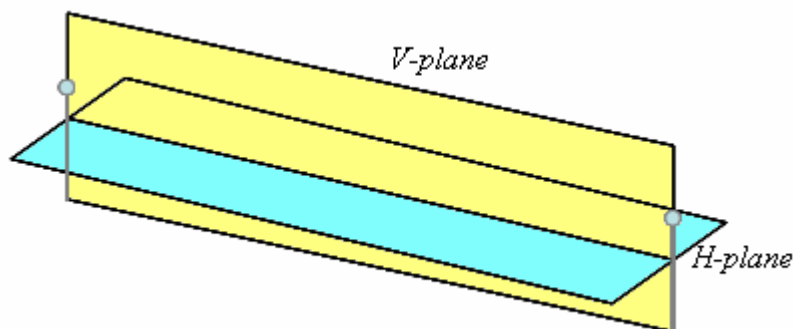
Figure 2.1 – Horizontal and vertical propagation planes.

• Vertical plane (*V-plane*): describes propagation in the plane containing the two antennas (transmitter and receiver);

• Horizontal plane (*H-plane*): describes propagation in the plane perpendicular to the vertical one and passing through the two antennas.

A classification of prediction models can be done using the following three categories:

1. Empirical models: express the electromagnetic field attenuation in relation to the distance between the antennas, and to some scene parameters (height of antennas, frequency, etc..) through approximate formulas, derived from empirical measurement results.

2. Statistical models: evaluate the electromagnetic field attenuation on the basis of an environment description by means of simple statistical indicators (average distance between objects, average height and average thickness of the walls existing in the scene, etc.) and taking into account only propagation phenomena occurring in the (vertical) plane containing the two antennas.

3. Deterministic models: more useful to calculate point to point propagation between two antennas, need a more accurate environment description, in terms of knowledge of geometric (position, orientation, thickness, etc.) and electromagnetic (attenuation, materials,

permittivity, etc.) characteristics of obstacles and sources. This detailed description is necessary in order to use the analytical functions, on which the models are based, directly derived from the *Maxwell equations*.

Both empirical and statistical models operate by means of average quantities, so they are strongly linked to a particular environment, or a sub-class of environments, that cannot be correctly generalized. On the other hand, they are fairly simple to be implemented and used, very fast and do not require neither powerful computers, nor with a big storage capability. The deterministic models, instead of the previous mentioned, are usually more complex and require the best resources, to be used; it is the price of having a more general method, that usually give predictions that better fit to the real physical phenomena.

Many studies have been developed in this research field, some for city applications [1-2], therefore outdoor, and some others, based on different criteria, best fit to work efficiently for indoor propagation.
Obviously, there is a trade off between accuracy and calculation speed, also among deterministic techniques. There are different ways to reach the best compromise, choosing to develop full-wave approach models[3-4], for example, or simpler 3D models based on ray tracing [5-9], in some cases combined with FDTD local analysis to reach more reliable results, or non-deterministic models [10-11].
Full wave methods, even if really accurate, can be used mostly for small coverage areas inside a building, because of excessive computational requirements. Models based on asymptotic solutions of Maxwell equations, on the other side, require less computational resources.
These are the reasons because the models more used in literature are, mostly, based on Geometrical Optics and its diffraction principles extensions.

2.1.1 Deterministic model

The more useful deterministic models, in large (in terms of wavelength) environments applications, are the so called ray optics methods, based on high frequency asymptotic solutions of *Maxwell equations* (*Geometrical Optics*)[5].

At high frequencies ($f \to \infty \Leftrightarrow \lambda \to 0$, for a given medium) the propagation in a lossless, time-invariant, isotropic medium can be modelled in terms of straight paths, or rays (see chapter 1). The limit of high frequency asymptotic solutions, for electromagnetic fields evaluations, is not such a constraint as it can appear at a first sight because, in the working hypotheses here considered, transmissions usually occur in the UHF (Ultra High Frequency, but only at frequencies between 1.9 GHz and 3 GHz) and SHF (Super High Frequency, only between 3 GHz and 6 GHz) bands.

Of course, the Geometrical Optics itself, even in a context of approximations, in terms of models, doesn't fully describe the distribution of electromagnetic fields in a generic environment.

GO only allows, in fact (if linear dimensions of obstacles in the scene are definitely higher than wavelength value), the evaluation of reflection and transmission contributions of the impinging rays at the obstacles themselves, without taking into account, for example, the possible presence of diffraction phenomena.

This omission, in general, can lead even to relevant errors. As we said in the previous chapter, in an outdoor environment it could easily happen that some areas in NLOS (usually not far from the source position), seeming wrongly not covered by the field distribution, after a more accurate calculation made taking into account the diffraction, would highlight the presence of unexpected field contributions.

In this work, despite the arguments just cited, any diffractive contributions are neglected because, for common types of materials, the fields generated by indoor sources are significantly confined within the environment. Positions reached by rays, only with paths in non-line of sight (NLOS), are thus really hard to find.

---

[5] See chapter 1

Neglecting diffractive contributions in indoors, usually, lead to significant errors only (sometimes) in closest areas to the transmitting antenna, where the electromagnetic field is anyway certainly sufficient to ensure the link. In field evaluation these errors are not reflected in significant errors, in determining the radio-coverage distribution, bringing, on the other hand, significant benefits in terms of computational load.

These assumptions and, of course, the related conclusions, are to be verified, by means of specific codes, implementing functions intended to calculate the diffractive contributions in the total field distribution evaluation. The results of these tests will be reported later.

For what concerns field levels calculation, the field contributions are evaluated deterministically in each point of the scene, and the total field value, related to the observation point, is the result of an incoherent sum. The following analysis explains why.

Let's consider a group of n field contributions $\mathbf{E_1}….\mathbf{E_n}$ coming on an observation point (that is, in a resolution cell whose dimensions are much greater than wavelength, containing the observation point); furthermore, consider each contribution as a plane wave, according to the G.O. approximations.
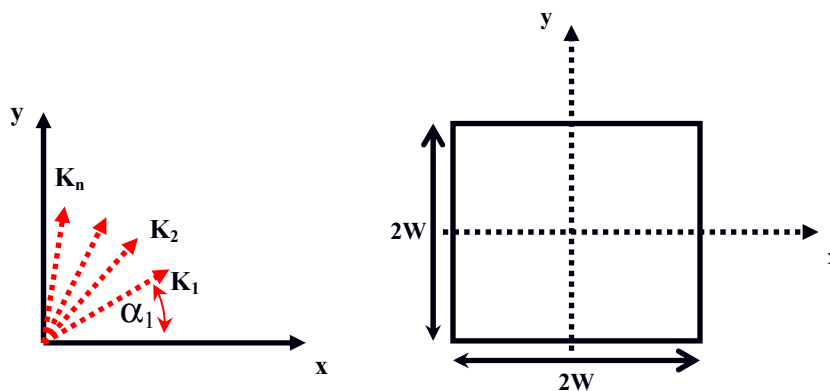

Figure 2.2   **Figure 2.3**

The analytical expression for the total electromagnetic field in the cell is (suppose all the contributions vertically polarized along the $\mathbf{z}$ axis, for example):

$$\mathbf{E} = \hat{\mathbf{i}}_z \sum_{n=1}^{N} E_n e^{-i\mathbf{\kappa}_n \cdot \mathbf{r}}$$

$$\mathbf{k}_n = k\cos\alpha_n \hat{\mathbf{i}}_x + k\sin\alpha_n \hat{\mathbf{i}}_y$$

(2.1)

where $\mathbf{k}_n$ is a (vector) *wavenumber*.

Suppose a square cell with a side dimension of 2W meters; the mean square value is:

$$\left\langle |\mathbf{E}|^2 \right\rangle_w = \frac{1}{4w^2} \int_{-w}^{w}\int_{-w}^{w} |\mathbf{E}|^2 dxdy$$

(2.2)

An expansion of the previous formula leads to:

$$\left\langle |\mathbf{E}|^2 \right\rangle_w = \frac{1}{4w^2} \int_{-w}^{w}\int_{-w}^{w} \mathbf{E}\cdot\mathbf{E}^* dxdy = \frac{1}{4w^2} \int_{-w}^{w}\int_{-w}^{w} \left(\sum_{n=1}^{N} E_n e^{-i k_n \cdot r}\right)\left(\sum_{n=1}^{N} E_n^* e^{-i k_n \cdot r}\right) dxdy = (2.3)$$

$$= \frac{1}{4w^2} \int_{-w}^{w}\int_{-w}^{w} \sum_{n=1}^{N}\sum_{m=1}^{N} E_n E_m^* e^{-i(k_n - k_m)\cdot r} dxdy =$$

$$\frac{1}{4w^2} \sum_{n=1}^{N}\sum_{m=1}^{N} E_n E_m^* \int_{-w}^{w}\int_{-w}^{w} e^{-ikx(\cos\alpha_n - \cos\alpha_m)} e^{-iky(sen\alpha_n - sen\alpha_m)} dxdy$$

(2.4)

As E_n and E_m don't depend, $\forall$ m, n, on integration variables, the previous expression becomes:

---

[6] $(\mathbf{k}_n - \mathbf{k}_m)\cdot\mathbf{r} = k(\cos\alpha_n - \cos\alpha_m)x + k(\sin\alpha_n - \sin\alpha_m)y$

$$\left\langle \left|\mathbf{E}\right|^2\right\rangle_w = \frac{1}{4w^2}\sum_{n=1}^{N}\sum_{m=1}^{N}E_n E_m^*\int_{-w}^{w}e^{-ikx\left(\cos\alpha_n-\cos\alpha_m\right)}dx\int_{-w}^{w}e^{-iky\left(sen\alpha_n-sen\alpha_m\right)}dy \quad (2.5)$$

and, solving each integral as below

$$\int_{-w}^{w}e^{-ikx\left(\cos\alpha_n-\cos\alpha_m\right)}dx = \left[\frac{e^{-ikx\left(\cos\alpha_n-\cos\alpha_m\right)}}{-ik\left(\cos\alpha_n-\cos\alpha_m\right)}\right]_{-w}^{w}$$
$$= \frac{2w\,sen\left[kw\left(\cos\alpha_n-\cos\alpha_m\right)\right]}{kw\left(\cos\alpha_n-\cos\alpha_m\right)} \quad (2.6)$$

we have that the mean square value is

$$\left\langle \left|\mathbf{E}\right|^2\right\rangle_w = E_n E_m^* \frac{sen\left[kw\left(\cos\alpha_n-\cos\alpha_m\right)\right]}{kw\left(\cos\alpha_n-\cos\alpha_m\right)}\frac{sen\left[kw\left(sen\alpha_n-sen\alpha_m\right)\right]}{kw\left(sen\alpha_n-sen\alpha_m\right)} \quad (2.7)$$

If we suppose $w \gg \lambda$, then the *sinc* functions values will be much lower than 1, except when m is equal to n (in these points the *sinc* value is equal to 1), so:

$$\left\langle \left|\mathbf{E}\right|^2\right\rangle_w \cong \sum_{n=1}^{N}\left|E_n\right|^2 \quad (2.8)$$

The previous is a good result. It justifies the choice to evaluate the total field, related to the observation point, using an incoherent sum of the different contributions coming.

Moreover consider that, in practice, it is difficult to collect hardly all the scene informations; in particular the walls positions, in the reference system, are not exactly known. This introduces randomness that may be taken into account by modelling a random phase with a uniform distribution.

Consider two of the field contributions above mentioned; given the previous hypotheses we can write, for example:

$$\begin{cases} \mathbf{E}_1 = \hat{\mathbf{z}}|E_{10}|e^{i\phi_1}e^{-i\mathbf{k}_1\cdot\mathbf{r}} \\ \mathbf{E}_2 = \hat{\mathbf{z}}|E_{20}|e^{i\phi_2}e^{-i\mathbf{k}_2\cdot\mathbf{r}} \end{cases} \qquad \angle E_n = \phi_n \approx U(-\pi,\pi) \qquad (2.9)$$

The sum absolute value will, then, be expressed as:

$$|E| = |E_{10}|\left|1 + \frac{|E_{20}|}{|E_{10}|}e^{i\phi}e^{-i(\mathbf{k}_2-\mathbf{k}_1)\cdot\mathbf{r}}\right| \qquad (2.10)$$

Suppose, now, $\mathbf{k}_1 = \dfrac{2\pi}{\lambda}\hat{x}$ and $\mathbf{k}_2 = \dfrac{2\pi}{\lambda}(\hat{x}\cos\alpha + \hat{y}\sin\alpha)$ $\qquad (2.11)$

the phase can be written as:

$$(\mathbf{k}_2 - \mathbf{k}_1)\cdot\mathbf{r} - \phi = \frac{2\pi}{\lambda}(x(\cos\alpha - 1) + y\sin\alpha) - \phi = -A - \phi \qquad (2.11)$$
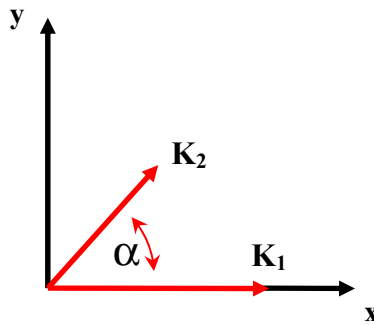

Figure 2.4

And the mean square value exactly is:

$$\left\langle \left| E_{1+} E_2 \right|^2 \right\rangle = \left| E_{10} \right|^2 + \left| E_{20} \right|^2 + 2 \left| E_{10} \right| \left| E_{20} \right| \left\langle \cos(A+\phi) \right\rangle =$$

$$= \left| E_{10} \right|^2 + \left| E_{20} \right|^2 + 2 \left| E_{10} \right| \left| E_{20} \right| \frac{1}{2\pi} \int_{-\pi}^{\pi} \cos(A+\phi) d\varphi = \left| E_{10} \right|^2 + \left| E_{20} \right|^2 \qquad (2.12)$$

Here the result is no longer an approximation, but an exact calculation.
The previous result justifies the choice to sum incoherently the various contributions coming into a single resolution cell.

At the working frequencies here used, a point few centimeters away from the source is already in the Fraunhofer zone; according to the *Friis transmission equation*, given the distance between transmitter and receiver, the effective area of the receiving Antenna and ERP power (Effective Radiated Power) or EIRP power (Effective Isotropic Radiated Power), the expressions for received power are the following:

$$received\ power = \frac{ERP}{4\pi r^2} A_{eff} = \frac{EIRP \cdot G_{NORM}(\vartheta,\varphi)}{4\pi r^2} A_{eff} \quad (2.12)$$

where A_{eff} represents the receiving antenna *effective area*, and G_{NORM} represents, along each possible direction, the (normalized) transmission gain.

On the basis of the results above an algorithm on them based, from which writing a field distribution prediction software for indoors, has been developed. In the following paragraphs are explained our steps towards this purpose.

2.2   A Ray-based propagation algorithm

To avoid unnecessary complexity of the (field) distribution prediction algorithm, during the definition of the modelling criteria for the indoor scenario, it has been necessary a rationalization.

Modelling all possible examples of building architecture would be clearly impossible, and the definition of a full 3D algorithm, operating in environments that can easily reach dimensions of the order of several hundred square metres of extension (or thousands of cubic metres of volume) is quite incompatible with the computing resources usually available. In most cases, anyway, this choice would hardly lead to significant results, in terms of useful information increase; from these assumptions it has been decided to neglect all the description elements unnecessary to obtain a representation of reality able to achieve sufficiently reliable predictions.
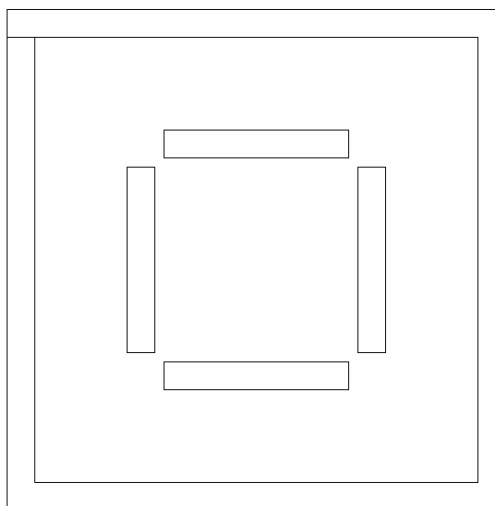

Figure 2.5 – 2D environment representation.

By abandoning the 3D representation in favor of a two-dimensional representation, the expressions that describe propagation functional models (and therefore the calculations results given by software

applications on them based) are thus more compact and light; in fact, through this choice, propagation phenomena descriptions can be simplified.

A second choice we can take, that directly follows the previous one, is to neglect refraction phenomena. Having agreed to model the propagation in a closed environment by using a ray approach (through the asymptotic solutions of the G.O.), given the distances involved in terms of paths and the transverse size of the objects intercepted by the rays themselves, it emerged that the deviations due to refraction, suffered by rays passing through a wall, can be considered negligible.
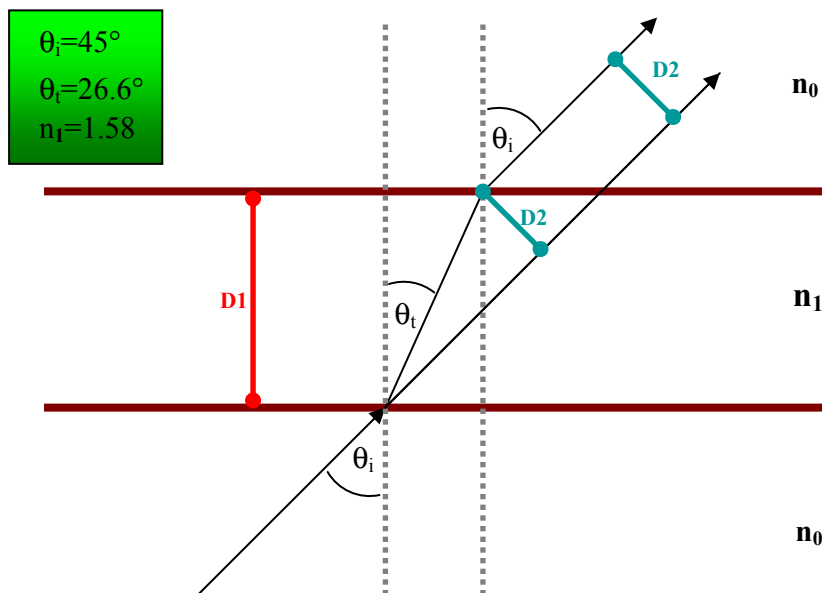

Figure 2.6 – A ray impinging on a wall.

Consider a classic example of interaction between a ray and an obstacle (*Figure 2.6*): an inner hollow bricks wall, with a 10-12 cm thickness, and a ray impinging the wall itself on the face below (note that is assumed to be able to model the electromagnetic field propagation through rays traced into the scene, following the GO principles), the incidence angle ϑ being equal to 45 degrees.

At the frequencies of our interest, before here specified, the relative permittivity, for this type of object, can be considered equal to about 2.5; applying here the *Snell's Law* we can also evaluate the angle θ_t in figure, its value being equal to about 26.6 degrees. This means that the D2 distance slightly exceeds 4 cm.

Moreover, consider that:

- The inner walls hardly exceed this thickness (while perimeter walls do not give rise to these problems at all, since we are interested to the indoor effects);

- The relative permittivity easily exceeds a value of 4 (in other words, in the exemple, we have a traslation of about 5 cm);

- Greater deviations are encountered, of course, when the incidence angles become wider and wider, and when materials have greater permittivity values. These conditions, on the other side, also lead to strong electromagnetic power attenuation beyond the obstacle; consequently, the error spread is severely restricted.

The choices so far taken allow a virtual collapse of the geometric representations of the walls that form and demarcate the scene in monodimensional objects, which can be easily described by means of the simple extremes coordinates. This is reflected also in a similar simplification in the input data structure of the algorithm.

From the physical phenomenon of microwave propagation we moved, therefore, to a description based on high frequency asymptotic models, coming to a representation of waves propagation made through ray tracings from a given source. At this point it is necessary to define an algorithm consistent with the choices above, in terms of propagation models.

Microwaves ⟶ *Geometrical Optics* ⟶ *Ray Tracing*

The most popular propagation algorithms, in scientific literature, are those known under the name of *ray-tracing* algorithms. Among the different ray-tracing versions, here two specific models will be described (**Figure 2.7**): the *inverse ray-tracing* and the *ray-launching* (or *direct ray-tracing*).
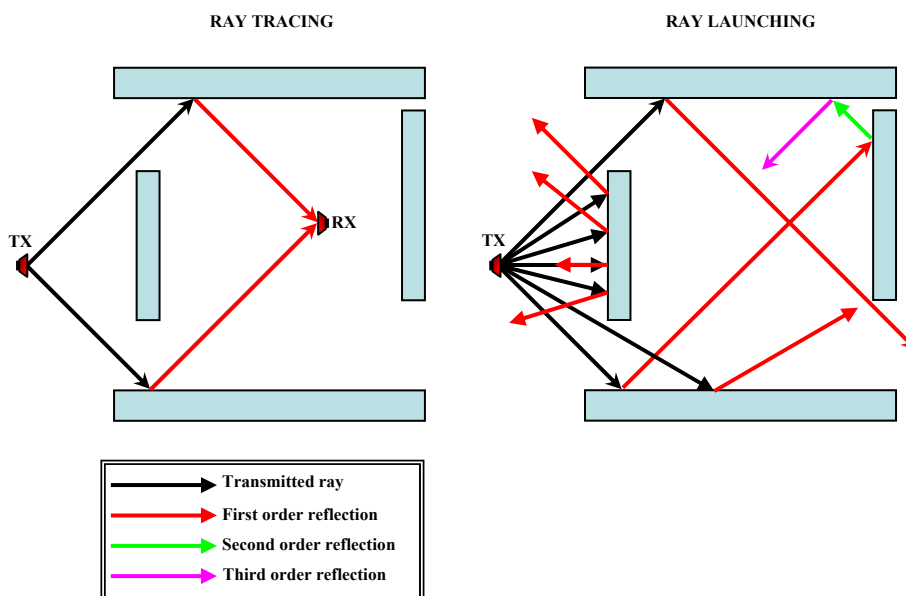
RAY TRACING   **RAY LAUNCHING**

Transmitted ray
First order reflection
Second order reflection
Third order reflection

Figure 2.7 – A ray-tracing and ray-launching representation.

• In the *inverse ray-tracing* (or simply *ray-tracing*) positions of source and receiver are fixed first, and then all possible paths that link these two points are followed. The total field value to the receiver is calculated from several incoming contributions, excluding all those associated with pathways that involve a great number of interactions (above a certain threshold a priori established) with obstacles existing in the environment. This condition is based on the following consideration: two contributions intercepted by the receiver, coming from different paths and covering the same distance, but involving a different number of collisions with the environment surfaces, have to be distinguished in terms of contributions weight. The contribution

resulting from an higher number of ray collisions is usually less significant, quantitatively, if compared to the other one.

• In the *ray-launching* approach the rays are traced from a source point, sweeping across the scene affected by the propagation, and are followed in all their interactions with the scene elements met on their way, up to overcome a certain field threshold value. The threshold is a user defined value, below which the contributions reflected by an obstacle are no longer considered significant. In this case the ray tracing is interrupted and the field value, at any point of the scene reached by the transmitted ray, is evaluated. This procedure is iterated on all the rays "launched" by the source.

The *inverse ray-tracing* is certainly the most widespread in the applications, because of its lightness (due to the used method, based on a "massive" contributions exclusion), and appears as the ideal approach for synthesis of fast algorithms (and thus for software implementation), making it possible to obtain results very quickly and, therefore, allowing the opportunity to run simulations several times in different operating conditions. The limit of this approach is the premise from which it derives, strictly speaking incorrect, that considers necessarily less relevant the contributions associated with pathways that involve a greater number of collision events with the walls.

This is actually not always true: a lot depends on the type of material that forms the obstacle (in particular in terms of permittivity, that depends on the working frequency), on its thickness and on the incidence angle; the first consequence, therefore, applying a criterion such as *inverse ray-tracing*, is the risk of exclusion of relevant contributions in the calculation of the total field.

Ray-launching, instead, does not provide for contributions elimination based on the number of events, but on the basis of the contributions values themselves, if they (being reflected by an obstacle) are below the established threshold. Following this approach we cannot fall into the same conceptual error as in the inverse ray-tracing, paying on the other hand the cost of a greater complexity.

In this case our choice has been, anyway, the ray-launching model, to achieve a greater accuracy in evaluating the electromagnetic field distribution on the scene.

The ray-tracing principle, applied in a environment to describe propagation effects is, as a matter of fact, a sort of angular sampling of the scene; this means that many points are not crossed by any ray (depending on the number of paths traced from the source, of course).

For this reason the scene is conceptually divided in adjacent angular sectors, called *anxels*, whose bisectors are represented by the rays traced from the source. Similarly, the scene is divided into field resolution cells; the anxels behaviour, in terms of propagation, is described, thus, by their bisectors (up to create, each other, a substantial identification), as the field value on a cell-center represents the field distribution throughout the cell itself.

The field calculation in a point of the scene is performed identifying, first, the cell to which the point belongs, then evaluating the propagation inside the anxel that covers the cell (to avoid any ambiguity, as when it is covered by more than one anxel, we assume that a cell "belongs" to that which covers the center of the cell itself) and finally calculating the distribution value in its center.

In general, the operating principle of these methods is to predict the total field received in a point of the scene as a superposition of the field contributions associated with each individual ray coming on that point; in perfect agreement with the previous assumptions, here, this superposition is performed via an incoherent sum of the impinging contributions. In the next section the details about the algorithm will be exposed.

2.2.1 Input data pre-processing

The input data, once defined by the operator, are firstly processed to become usable by the analysis block of the prediction tool; the functional blocks below described perform this function.

— *AntennaSetup_reader:*
Through this routine, the analysis block extracts from the input database all the typical parameters in the *SetupAntenna* table, where are stored the antenna settings (tilt, gain, power, etc.).

— *AntennaDiagram_reader*:
It is the module that imports in the analysis block, for each source, the gain values in dB, angle by angle, normalized on the maximum gain value. These values are present in the *AntennaDiagram* table.

— *Map_reader*:
This procedure transfers to the analysis block informations regarding some significant scene parameters (scale, offset) saved in the *Cartaceo* table.

— *Delta*:
This procedure receives the output resolution and the size of the scene chosen by the operator as input data. The aim of this functional block is to calculate the anxel angular extension, without leaving "holes" in the scene after the scene sweeping procedure.

$$\varphi_1 = arctg(H/L)$$

$$\varphi_2 = arctg\left(\frac{H}{L-R}\right)$$

$$\varphi' = \varphi_2 - \varphi_1$$

$$N° of \ anxels = floor(360/\varphi')$$
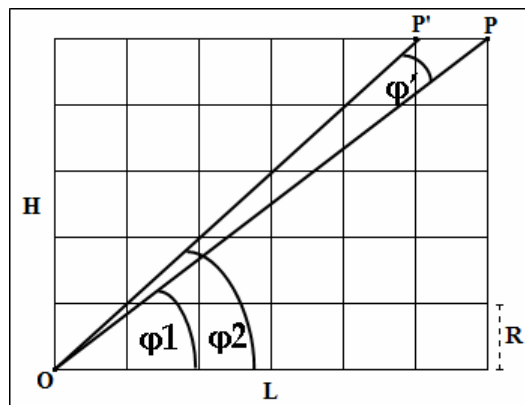
$$\Delta\varphi = 360/N° of \ anxels$$

Figure 2.8 – Anxel definition.

In Figure 2.8 is exemplified the method used to define a whole number of anxel in which can be splitted the scene, depending on scene dimension and cell resolution.

The principle is to identify the two extremes of the scene diagonal (*O* and *P*) first, and trace a segment connecting each other; in the same way another one is traced, joining point *O* with the other end of the same cell (*P′*), containing either points P and P′.

Later, through simple trigonometric calculations, the anxel nominal angular extent is evaluated, as a function of φ_1 and φ_2. The effective extent $\Delta\varphi$ is determined by evaluating the whole anxel number necessary to cover 360°, once set as the anxel dimension to φ' and then calculate $\Delta\varphi$ as the ratio between the extension 360° and the actual number of anxels.

— *Diagram_interp*:

Its task is to reconstruct, from the radiation diagram cuts (horizontal and vertical) and through interpolation, the whole three-dimensional radiation diagram. When the antenna is not in a vertical position, then, the implemented algorithm modifies the diagram, conceptually using the analytical procedure below described.
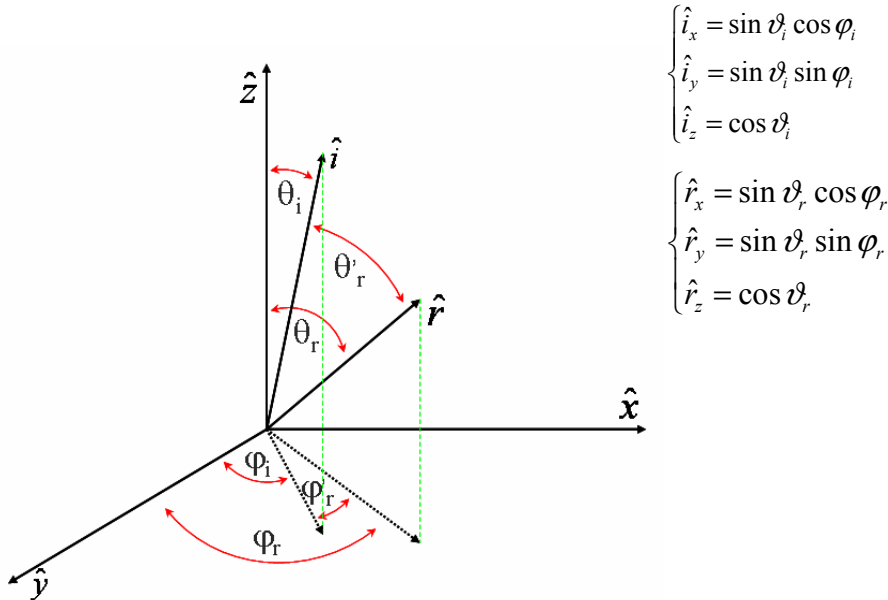

$$\begin{cases} \hat{i}_x = \sin\vartheta_i \cos\varphi_i \\ \hat{i}_y = \sin\vartheta_i \sin\varphi_i \\ \hat{i}_z = \cos\vartheta_i \end{cases}$$

$$\begin{cases} \hat{r}_x = \sin\vartheta_r \cos\varphi_r \\ \hat{r}_y = \sin\vartheta_r \sin\varphi_r \\ \hat{r}_z = \cos\vartheta_r \end{cases}$$

Figure 2.9 – Diagram reconstruction

$$\hat{i} \cdot \hat{r} = \sin \vartheta_i \sin \vartheta_r \cos(\varphi_r - \varphi_i) + \cos \vartheta_i \cos \vartheta_r \qquad (2.13)$$

$$\begin{cases} \varphi'_r = \varphi_r - \varphi_i \\ \vartheta'_r = \cos^{-1}(\hat{i} \cdot \hat{r}) \end{cases} \longrightarrow NewGain(\varphi_r, \vartheta_r) = OldGain(\varphi'_r, \vartheta'_r)$$

The outlined procedure describes how to evaluate the antenna diagram gain in different directions (angle by angle identified by an unit vector $\hat{r}$), when its axis is moved from the direction identified by the z axis, to another identified by î unit vector.

— *Analysis_block_Setup*:
This procedure transfers to the analysis block informations regarding some significant scene parameters (output resolution, reflection treshold, scene dimensions) saved in the table *AnalysisblockSetup*.

— *JoinWalls_Materials_ reader*:
It collects all the information and data, related to obstacles dielectric and geometric properties, from two different tables (*Walls* and *Materials*).

2.2.2 Output data representation

To simulate a field distribution through softwares (as to simulate any other function of space), in a given environment, necessarily means to proceed in some way to a space sampling of the scene; this will inevitably influence the output representation, depending on the performed discretization.
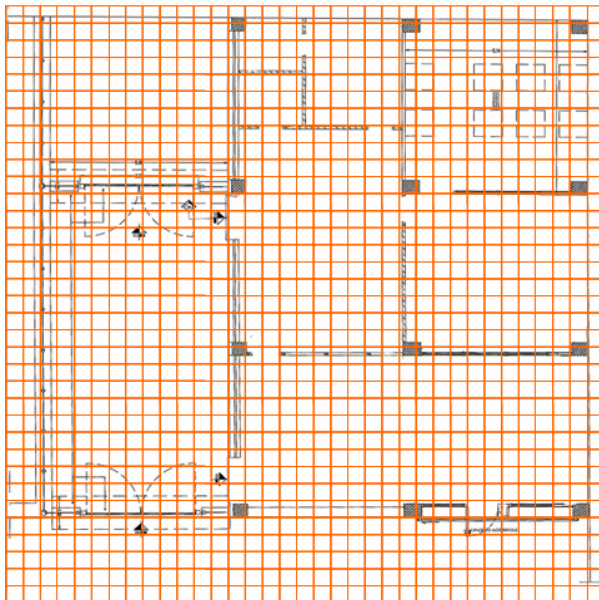In this case, a sampling grid is applied on the scene, with appropriate step chosen by the user, according to his needs, in terms of field resolution output.

Figure 2.10 – Scene subdivision in resolution cells.

The grid divides the scene into adjacent squared resolution cells (*Figure 3*), whose side having size equal to the chosen sampling step, within which is assessed the electromagnetic field value.

0.000000	0.000000	0.000000	0.000000	0.000000	0.000000	0.000000	0.000000	0.000000	0.000000
0.000000	0.000000	0.000000	0.000000	0.000000	0.000000	0.000000	0.000000	0.000000	0.000000
0.000000	0.000000	0.000000	0.000000	0.000000	0.000000	0.000000	0.000000	0.000000	0.000000
0.000000	0.000000	0.000000	0.000000	0.000000	0.000000	0.000000	0.000000	0.000000	0.000000
0.000000	0.000000	0.000000	0.228007	0.232243	0.224043	0.228522	0.244890	0.250185	0.254519
0.259380	0.264030	0.270825	0.276606	0.280128	0.285453	0.291804	0.000000	0.000000	0.000000
0.000000	0.000000	0.422951	0.380163	0.367465	0.355461	0.343581	0.333797	0.325445	0.316747
0.308878	0.301365	0.294999	0.288537	0.282891	0.277142	0.272094	0.000000	0.000000	0.000000
0.000000	0.000000	0.000000	0.000000	0.000000	0.000000	0.000000	0.000000	0.000000	0.000000
0.000000	0.000000	0.000000	0.000000	0.000000	0.000000	0.000000	0.000000	0.000000	0.000000
0.000000	0.000000	0.000000	0.000000	0.000000	0.000000	0.000000	0.000000	0.000000	0.000000
0.000000	0.000000	0.000000	0.000000	0.000000	0.000000	0.000000	0.000000	0.000000	0.000000
0.000000	0.000000	0.000000	0.000000	0.000000	0.000000	0.000000	0.000000	0.000000	0.000000
0.000000	0.000000	0.000000	0.000000	0.000000	0.000000	0.000000	0.000000	0.209154	0.212411
0.215820	0.207646	0.211195	0.215113	0.219042	0.223346	0.227723	0.285407	0.289007	0.248751
0.254440	0.258356	0.262934	0.264561	0.268112	0.000000	0.000000	0.000000	0.000000	0.000000
0.000000	0.000000	0.000000	0.000000	0.392235	0.355741	0.344802	0.333712	0.324739	0.316122
0.309069	0.301731	0.294654	0.288224	0.282692	0.276792	0.271834	0.266690	0.262215	0.257568
0.253504	0.249621	0.000000	0.000000	0.000000	0.000000	0.000000	0.000000	0.000000	0.000000
0.000000	0.000000	0.000000	0.000000	0.000000	0.000000	0.000000	0.000000	0.000000	0.000000
0.000000	0.000000	0.000000	0.000000	0.000000	0.000000	0.000000	0.000000	0.000000	0.000000
0.000000	0.000000	0.000000	0.000000	0.000000	0.000000	0.000000	0.000000	0.000000	0.000000
0.000000	0.000000	0.000000	0.000000	0.000000	0.000000	0.000000	0.000000	0.000000	0.000000
0.000000	0.000000	0.000000	0.194318	0.196922	0.199630	0.191611	0.194391	0.197292	0.200497
0.203667	0.207135	0.210615	0.214293	0.218132	0.222047	0.269365	0.275648	0.281932	0.285511
0.245934	0.249359	0.251909	0.000000	0.000000	0.000000	0.000000	0.000000	0.000000	0.000000
0.000000	0.000000	0.000000	0.000000	0.000000	0.000000	0.367347	0.334308	0.325043	0.316738
0.308667	0.301401	0.294337	0.288619	0.282538	0.276613	0.271752	0.266601	0.262200	0.257387
0.253385	0.249153	0.245493	0.241984	0.238264	0.235034	0.231928	0.000000	0.000000	0.000000
0.000000	0.000000	0.000000	0.000000	0.000000	0.000000	0.000000	0.000000	0.000000	0.000000

Figure 2.11 – Output data matrix.

These cells are represented, in terms of distribution, by their centre; this means that for any point within a cell, the value of associated field is the same of that in the centre. The distribution is represented with a finite number of values, recorded inside a matrix (*raster*) whose size depends on the scene extension in both width and length, and on the chosen output resolution.

The output matrix (*Figure 4*) is the basis on which starting the distribution representation. Every element, linked with a biunique relationship to the coordinates (on the basis of a given reference system established) of a cell-centre, is represented graphically in a false colors scale depending on values in the matrix contained; the output will be a map, in which areas uniform in color will consist of one or more adjacent cells, characterized by a single value of field/power (in *Figure* 3.3 there is an example of received power distribution, in dBm, represented in false colors).

2.2.3 Electromagnetic propagation evaluation

The definition of calculation algorithms result, as well as from electromagnetic models characteristics, from computational geometry considerations aimed to minimize computational load and achieving an high (as much as possible) accuracy.

The algorithms to be used were developed to reach optimal calculation criteria for complex environments applications, allowing to repeat simulations changing the radiating elements position, or to perform multiple simulations (with more source points simultaneously lighting). A brief outline of the algorithm core, structured in macro-blocks, is reproduced below (*Figure 2.12*):
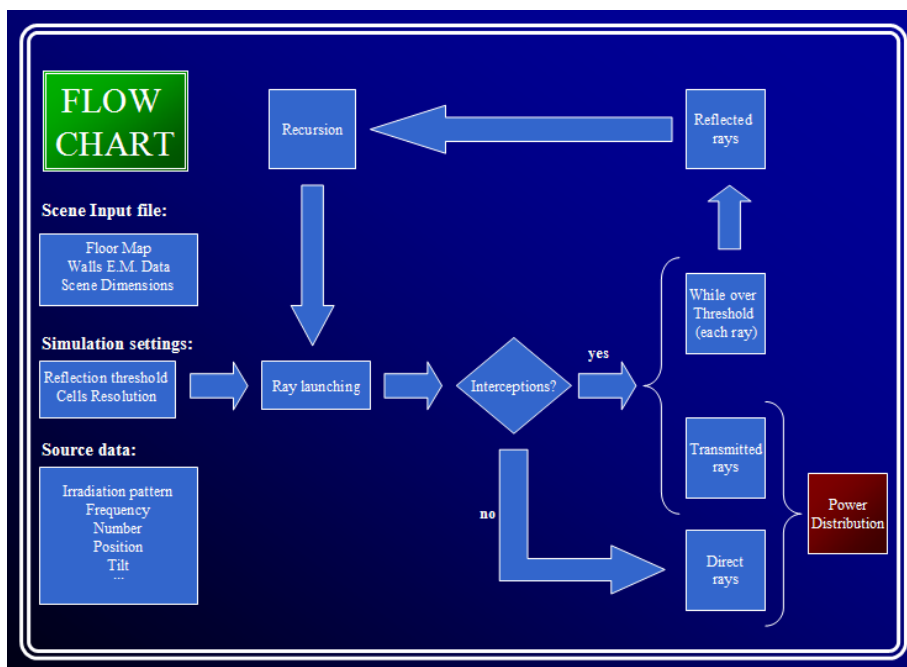
Figure 2.12 – Algorithm rationale

The algorithm is designed to be intrinsically recursive: the analysis block in Figure 2.12 represented acts on a data entry set (which will be

soon specified) that includes the source, and calls recursively itself on new sources (image sources) during the elaboration generated, until the recursion interruption condition.

The algorithms, represented in macroblocks depicted in Figure 2.12, are described below, using the same names as the routines from them implemented, for easier identification.

— *Cycle*:

All data entry and settings are acquired (using the previously introduced sub-routines) by this module, which performs the function of main program block calculation; its task is making calls to appropriate sub-acquisition modules, reconstructing the sources and the building characteristics and sending them to the analysis block (the core routine). The inputs include information (in electromagnetic and geometric terms) on antennas and objects existing in the scene (walls, pillars, doors, etc.), on number of sources, on output resolution and on the scene size itself.

The module sets, depending on the scene dimensions (extension in both width and length) and the chosen sampling rate for the output (step), the matrixes necessary for data production and storage. Later, the module starts defining and processing sources data, evaluating wavelength, the receiving antenna *effective area* and the *radiation diagram*, calling the *Diagram_interp* block. Before calling *Analysis block,* which is responsible for carrying out electromagnetic field (or power) distribution calculations, TE and TM field components are separated to provide input, according to the antenna settings.

Downstream of the *Analysis block* call, *Cycle* evaluates the received power in dBm starting from the receiving antenna effective area and from the total density power (default physical quantity evalued and registered in the output matrixes). In a final step it collects all data about all contributions delays, by the *Analysis block* subroutines calculated, generated during the field propagation on the scene. This step is necessary to perform the *delay spread* calculation in each cell resolution of the environment. Finally, the algorithm provides a final step for saving data on file, exploiting the output subroutine.

NOTE: The algorithm provides, as pointed out previously, the

management of multiple simulations, in other words with more sources simultaneously present in the scene. When there is more than one source in the scene, it can be computed the overall power distribution matrix, useful for coverings assessment on very large environments (when such a distribution has got physical sense, of course).

— *Analysis block*:

It is the real calculation core of the system; it is based on a recursive approach, which carries out the recursions depending on the sources actually present in the scene (real or image ones). The aim is the electromagnetic coverage calculation in an indoor environment, once given its geometric characteristics, that is to say the walls thickness and extremes coordinates, and electromagnetic characteristics of the materials (specifically the complex material permittivity of the walls).

The algorithm first provides a (three dimensional) anxel matrix initialization, in which informations about each anxel, necessary for the calculations, should be recorded. After this step it starts calculating "image points" (image sources positions) related to obstacles registered in the walls data base, through the *Image* routine, and intersections, by means of *Ray_launch*, by executing it iteratively on all obstacles. The next step requires a transformation applied on the intersections coordinates (centered on local source) [7], from cartesian to polar system, a deletion of all *ghost* [8] *intersections*, an ordering on those remaining, by distance from the source, and another coordinates transformation applied on the latters, to the original coordinate system. The ordering phase, useful to assess the transmitted field attenuation over the obstacles, uses a bubble sort-like algorithm, implemented in the *BubbleSort_matrix* module, while the coordinate transformations are executed by the vector conversion modules *Xy2rofi_matrix* and *Rofi2xy_matrix*.

After these preliminary actions the algorithm starts the calculation procedure for power distribution (see Formula 2.12) in terms of free space propagation (without, therefore, taking into account the obstacles presence effects), using the *Field_matrix_evaluation*

---

[7] Real or image source, depending on the level of recursion running.

[8] The intersections on the walls between the source, if it is an image source, and the wall against which it is the image.

procedure. To assess the attenuation of the transmitted field over obstacles, a special block was developed (*Events_manager*) that, using *ad hoc* coordinate conversion (scalar) modules (X*y2rofi* and *Rofi2xy*), iteratively calculates the correct attenuation, to be applied to the free space field, in each cell center beyond one or more obstacles. This attenuation is calculated by the *Field_evaluation_T* procedure.

At this point, the field distribution is calculated and the algorithm switches to a second part of the calculation, which provides for sources image [9] generation (starting from the already calculated image points and from local source informations), on which it calls itself recursively.
The algorithm uses a similar procedure, in case of real source and image source, but differs slightly the two cases, to make easier the calculations and the information research phase in the anxel data matrix. In this stage, for each anxel (or image point) the reference system is reversed, so as to properly get the irradiation diagram gain values associated to the locally generated source, starting from the real one; later, using an approach similar to that previously mentioned in the free space propagation calculation for the distribution matrix, through a combined use of *Events_manager* and *Xy2rofi*, EIRP image source power is evaluated, attenuating appropriately (with Fresnel [10] coefficients) the EIRP real source power. At this point all the information on the new source is acquired, and the final step before the recursion starts, on the so generated source, is to identify the area of the scene enlightened by it, in the new instance, except the area between the image point position and the wall to it associated ("image wall"). *Field_evaluation_gamma* is the block that detects this area and sends this information, together with the source data, to the *Analysis block* new instance; it will correct its local distribution matrix, while using the module *Field_evaluation_T*. For each image source generated, *Analysis block* calculates the delays matrixes (in free space and into the walls) necessary for delay spread evaluation, also using the *Field_evaluation_T* procedure. Then it calls itself with the new

---

[9] Not really image sources, because they generate only one anxel. So if the source image itself radiates N anxel, the
   algorithm generates, in reality, N sources geometrically superposed.
[10] For TE and TM components, respectively.

data entries, perpetuating thus recursion (up to the interruption condition, assessed by *Events_manager*). The output is a matrix that will be added to the "mother" local distribution, and so on, recursively, till the end of computation.

 — Outputs
It is the module that fetches the outputs matrix and saves results in two output files, one in binary form and a second one, which is a copy in text format, easily accessible with any text editor.

 — Image
Starting from local [11] source and walls terminations coordinates, in the scene, it calculates the coordinates of the image points with respect to these walls. The procedure involves calculation of the slope of the line passing through the source and perpendicular to the wall [12] axis.

 — Ray_launch
Its role is to build the vector of intersections, with one of the walls, of the rays coming from the source. To carry out this function it uses the modules X*y2rofi* and *Anxel_ray_launching*: it is called by *Analysis block* for each wall of the scene.

 — Xy2rofi
It performs a simple coordinates transformation on a single point (in this sense, therefore, is a scalar transformation), from a cartesian reference system with assigned source to a polar system centered in another point.

 — Rofi2xy

It performs a simple coordinates transformation on a single point (in this sense, therefore, is a scalar transformation), from a polar system centered in a point to a Cartesian reference system with assigned source.

 — Anxel_ray_launching

---

[11] "Local" means that it is the source, in the current recursion instance.

[12] Straight through the two extreme points that identify the wall in the model.

It implements calculation of the intersection of a ray with the longitudinal axis of a wall; it exploits previously described modules for single point coordinates transformation.

 — *Xy2rofi_matrix*
It performs a coordinates transformation on a certain number of points (in this sense, therefore, is a vectorial processing), from a Cartesian reference system with assigned source to a polar system centered in another point.

 — *Rofi2xy_matrix*
It performs a coordinates transformation on a certain number of points (it is a vectorial processing, like the previous one), from a polar reference system centered in a point anywhere on the scene, to a cartesian reference system with assigned source.

 — *BubbleSort_matrix*
It orders the rows of a matrix, with reference to the values of one of the columns, using a *bubble sort*-like approach.

 — *Field_matrix_evaluation*
It is the module that evaluates the field distribution in free space, given the source geometric and electromagnetic information. Converts all the scene cell-center coordinates in a polar reference system centered in the source, so as to associate an anxel to each center. Combining the so obtained coordinates matrix with the array in which the irradiation diagram is registered, is possible, therefore, to go back to the correct attenuation values, to be applied (in each direction) to the source EIRP power. Once carried out these operations, the module transforms again the cell center coordinates in a Cartesian reference system, rising to calculate the power distribution on the scene.
Informations about free space delays are also provided by this block.

 — *Events_manager*
It has been designed to handle both geometric and electromagnetic interactions of rays with obstacles in the scene. For each item associated to the current source, and stored in the intersections array,

it calls appropriate modules to perform calculations about the field by the surface reflected and the point of impact coordinates; if the reflected field value does not exceed the preset threshold, the *Events_manager* elide the corresponding intersection from the list of "image sources generators" [13], inhibiting the generation of the reflected ray.

— Reflection

It is the procedure realized to evaluate Fresnel coefficients on double interface stratified structures (air - wall - air), using the Phasors Domain mathematical formalism.

— Field_evaluation

This module role is to calculate the field distribution in free space, given informations on geometric and electromagnetic properties of the source; it is based on the same theoretical basis on which develops the *Field_matrix_evaluation* module algorithm. The difference is that the calculation is not made on a matrix, as in the previous, but on a single point of the scene, using also the coordinates "scalar" transformation modules before described, to carry on the procedure.

— Field_evaluation_T

This module role is to calculate (working on matrixes) the attenuation suffered by an anxel field contribution, due to propagation over an obstacle, in all cell centres covered by it beyond the obstacle itself. It calls other modules to convert cell centres (and also the intersection point) coordinates in a polar reference system centered in the source, so as to associate an unique anxel to each cell centre. Immediately later it creates a mask on the scene, isolating only cells in the anxel under consideration contained. On these cells it evaluates the attenuation value due to ray passage through the obstacle and then, once carried out these operations, it calls other modules to convert cell-centres positions in Cartesian coordinates, rising to calculate real (attenuated) power distribution, on the scene by the anxel illuminated. Informations about walls space delays on each single ray are also provided by this block.

---

[13] Starting point to evaluate the image point position.

 — *Field_evaluation_gamma*
It is a module called by *Analysis block* to calculate the scene area
which will be illuminated by the image anxel, in the new *Analysis
block* instance; in particular it calculates the scene portion between the
image position and the position of the wall respect to which it is the
image of its "mother source" [14]. *Field_evaluation_gamma* detects that
area and sends this information, together with source data, to the new
Analysis block instance, which will erase contributions to it associated
in its local distribution matrix.

---

[14] Source starting from which it is calculated the image.

References

[1] K.R. Schaubach, N.J. Davis IV and T.S. Rappaport, A ray tracing method for predicting path loss and delay spread in microcellular environments, 42nd IEEE Vehicular Technology Conf. , Denver, Co, May 1992, pp. 932-935.

[2] G. Liang, H.L. Bretoni "A new approach to 3-D ray tracing for propagation prediction in cities", IEEE Trans. Antennas Propagat., vol 46, pp. 853-863, 1998.

[3] C.-P. Lim, J. L. Volakis, K. Sertel, R. W. Kindt, and A. Anastasopoulos, "Indoor propagation models based on rigorous methods for site-specific multipath environments", IEEE Transactions on Antennas and Propagation, vol. 54, no. 6, pp. 1718-1725, 2006.

[4] Zygiridis, T.T.; Kosmidou, E.P.; Prokopidis, K.P.; Kantartzis, N.V.; Antonopoulos, C.S.; Petras, K.I.; Tsiboukis, T.D. "Numerical modeling of an indoor wireless environment for the performance evaluation of WLAN systems", IEEE Tran. On Magnetics, 2006, Vol. 42, No 4, April 2006, pp. 839-842.

[5] M. Porebska, T. Kayser, and W. Wiesbeck, "Verification of a hybrid ray-tracing/FDTD model for indoor ultra-wideband channels," in 10th European Conference on Wireless Technology, Munich, Germany, Oct. 2007.

[6] J. Diskin and C. Brennan "An Efficient Ray-Tracing Image Removal Algorithm for Indoor 3D Radiowave Propagation Modelling", in press, The first European Conference on Antennas and Propagation (EuCAP 2006), Nice France, November 2006.

[7] M. Allegretti, L. Coppo, R. Notarpietro, G. Perona, "An enhanced 3D ray tracing algorithm for indoor EM propagation", XVI RINEM, Genoa 18-21 Sept, 2006

[8] Alves, F.A.; de Albuquerque, M.R.M.L.; da Silva, S.G.; dapos;Assuncao, A.G. "Efficient ray-tracing method for indoor propagation prediction", Microwave and Optoelectronics, 2005 SBMO/IEEE MTT-S International Conference on Volume , Issue , 25-28 July 2005 Page(s): 435 – 438

[9] G.E.Athanasiadou, A.R.Nix, J.P.McGeehan, 'A new 3D Indoor Ray Tracing model with particular reference to predictions of power and RMS delay spread', IEEE PIMRC '95, pp. 1161-1165, Toronto, Canada, September 1995.

[10] K. W. Cheung, J. H. M. Sau, and R. D. Murch. A new empirical model for indoor propagation prediction. IEEE transactions on vehicular technology, v. 47, no. 3, August 1998, p. 996-1001

[11] D.A.M. Saleh and R.A. Valenzuela, "A statistical model for indoor multipath propagation", IEEE J. Sel. Areas Commun., vol.SAC-5, no.2, pp.128–137, 1987.

Chapter 3

Simulations and measurements

In this chapter are presented results of simulations in canonical conditions, and also of other simulations in more realistic environments with real sources, too. Moreover are shown results of a set of measures, aimed at assessing the correctness of approximations made in propagation analytical models and in environmental representation. At the end of the chapter a phase of models modification is also described, necessary to verify *ex post* the consequences, on the algorithms accuracy, of having neglected the diffraction influences in indoor environments total field distribution.

3.1   Simulations in canonical conditions

Once implemented a software, starting from models here described, to achieve the first simulations and make a first check on their results (basically in qualitative terms, in a first step), it was used an omnidirectional antenna model (see Figure 3.1) with unit gain along the maximum direction.

The virtual environment here created to perform simulations (see Figure 3.2) is a rough description of the first floor of *DIBET*[15], in Via Claudio 21 (Naples). The walls constituting the different rooms and corridors were described as determined during the algorithm definition, in terms of thickness, dielectric properties of the material and extremes geometric position in the scene.

---

[15] Dipartimento di Ingegneria Biomedica, Elettronica e delle Telecomunicazioni, Università degli Studi di Napoli Federico II.
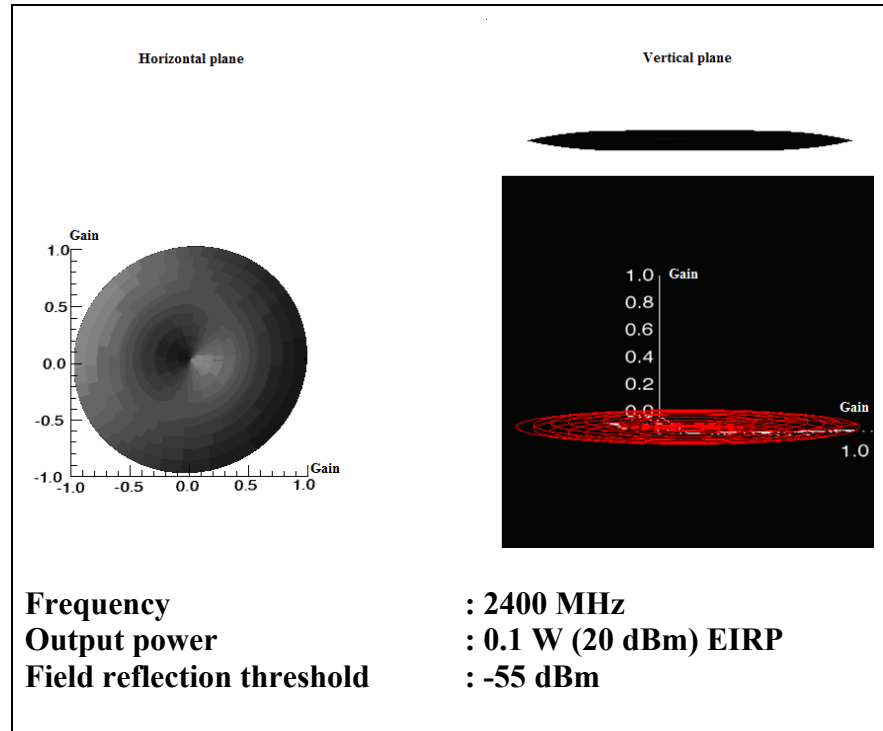
Figure 3.1 - Canonical antenna characteristics.

The perimeter walls have the following characteristics:

➢ *Thickness: 0.35 m*
➢ *Permittivity (real part): 5.2*
➢ *Conductivity: 0.10 S/m*

The vertical inner walls have the following characteristics:

➢ *Thickness: 0.01 m*
➢ *Permittivity (real part): 2.0*
➢ *Conductivity: 0.07 S/m*

The horizontal inner walls have the following characteristics:

➤ *Thickness: 0.1 m*
➤ *Permittivity (real part): 4.0*
➤ *Conductivity: 0.05 S/m*

The source position is reported, in figure, using a small red hexagon.
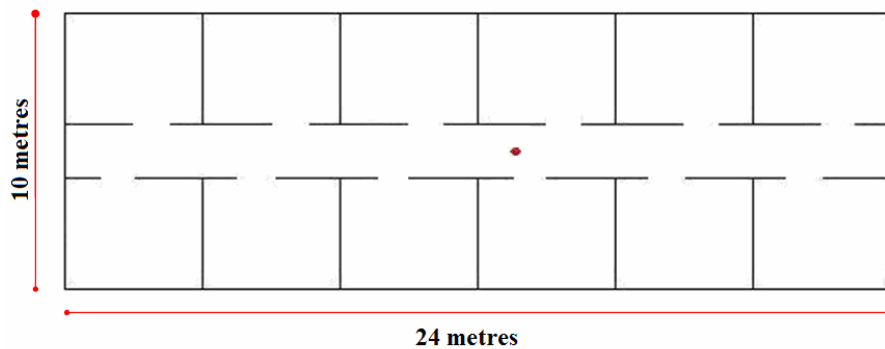
Figure 3.2 – DIET planimetry, floor one, source in the first position.

The simulation result is represented in Figure 3.3: the scene covers a total area of 26m x 12m, and the floor covers 24 meters in width and 10 in length of this area.
The simulator calculates, once known all significant parameters, the power density distribution on the scene defined; what is displayed in Figure 3.3 is the evaluated power distribution (in dBm), assuming an unit gain receiving antenna.

It is clear that the simulator behaves as expected, showing power flows through the walls openings (point **a**, in the figure) and, on the other side, darker bands (point **b**, in the figure) due to the lack of reflected contributions through the openings themselves.

Area:
Lower left corner: (0.0, 0.0) / Upper right corner: (26, 12)
Resolution   : 0.25 m

Values scale in dBm

Source position	: (14, 6.0) m
Frequency	: 2400 MHz
Max. output power (downlink)	: 0.1 W (20 dBm) EIRP
Reflection threshold	: -55 dBm
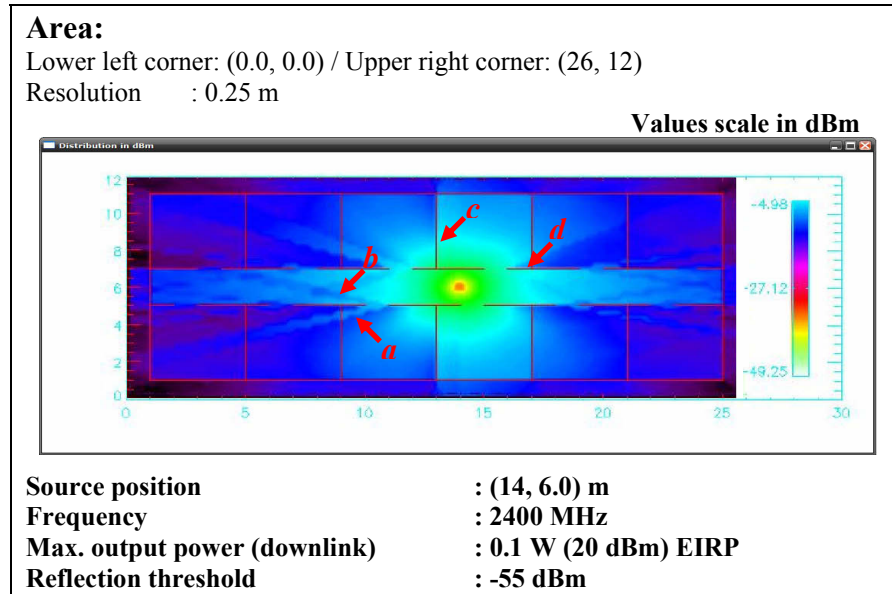
Figure 3.3 – Power distribution, the source in the first position.

Another interesting point is the dependence from incidence angles that, in fact, strongly influence the Fresnel coefficients. This behaviour can be seen in point *c* and in point *d*, in Figure 3.3: where incidence angles are larger, the power amount able to pass through the obstacles decreases conspicuously; the phenomenon is even more visible putting the source closer and closer to a wall, as in Figure 3.4 and in Figure 3.5 (points *e*, *f*, *g*, *h*).

24 metres
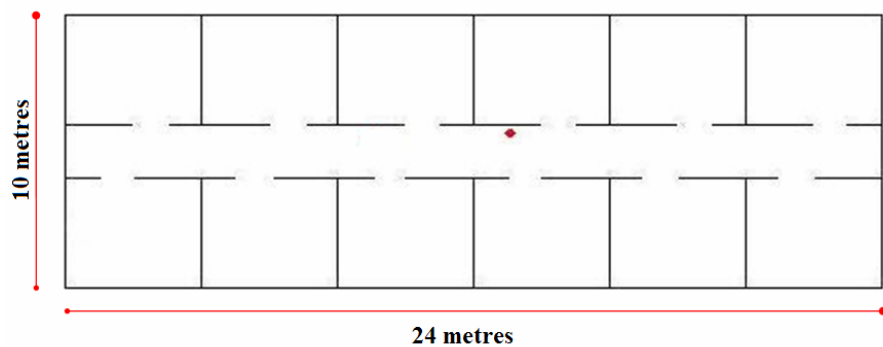
Figure 3.4 - DIET Planimetry, floor one, source in the second position.

Area:
Lower left corner: (0.0, 0.0) / Upper right corner: (26, 12)
Resolution   : 0.25 m

Values scale in dBm

Source position	**: (14, 6.9) m**
Frequency	**: 2400 MHz**
Max. output power (downlink)	**: 0.1 W (20 dBm) EIRP**
Reflection threshold	**: -55 dBm**
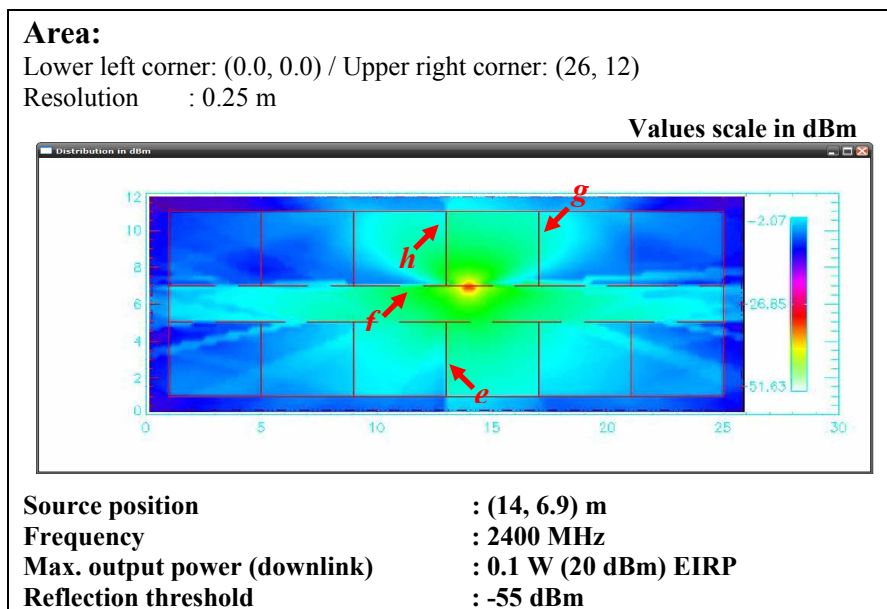
Figure 3.5 - Power distribution, the source in the second position.

If we want to analyze what is the channel behaviour in the time domain, the algorithm incorporate functions able to calculate the *rms delay spread*, as illustrated in chapter 1. For a canonical scene, like the corridor in Figure 3.6, the result is shown in Figure 3.7. The values refer to a "spatial" delay spread σ_s (according to equations 3.1 and 3.2), that can be converted to the proper rms delay spread dividing the matrix values by the light speed value in vacuum.

$$S_0 = \sum_{n=1}^{N} A^2{}_n s_n \bigg/ \sum_{n=1}^{N} A^2{}_n \qquad (3.1)$$

$$\sigma_s = \sqrt{\sum_{n=1}^{N} A^2{}_n \left(s_n - S_0\right)^2 \bigg/ \sum_{n=1}^{N} A^2{}_n} \qquad (3.2)$$

S_0 is the mean spatial delay[16], while s_n is a contribution spatial delay.

---

[16] Here, the spatial delay is intended as the overall contribution path extension, during its propagation in the environment.

Area:
Lower left corner: (0.0, 0.0) / Upper right corner: (39.5, 14)
Resolution   : 0.5 m   **Values scale in dBm**

Source position	**: (2.90, 5.66) m**
Frequency	**: 2045 MHz**
Max. output power (downlink)	**: 14 dBm EIRP**
Reflection threshold	**: -70 dBm**
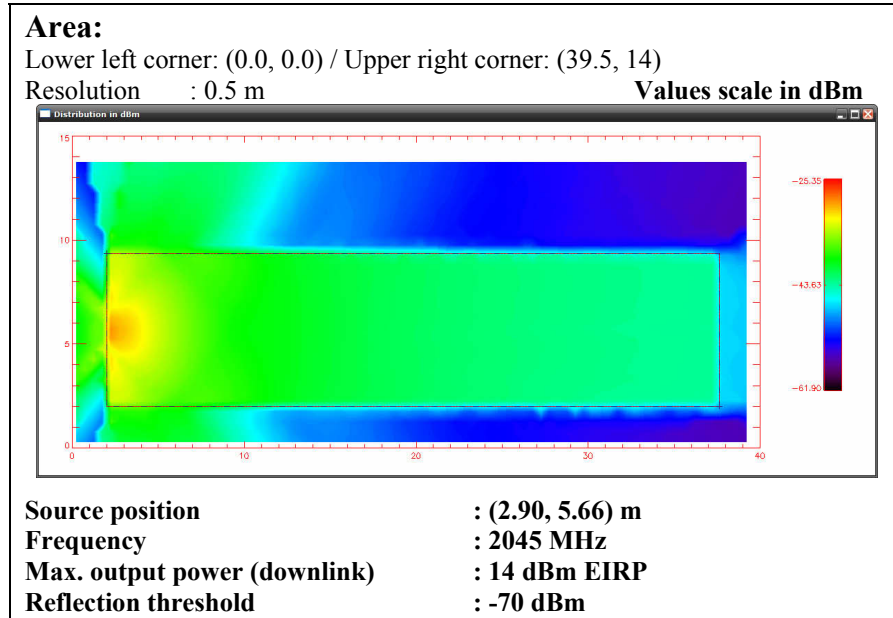
Figure 3.6 – Power distribution in a corridor.

Area:
Lower left corner: (0.0, 0.0) / Upper right corner: (39.5, 14)
Resolution   : 0.5 m   **Values scale in m**

Source position	**: (2.90, 5.66) m**
Frequency	**: 2045 MHz**
Max. output power (downlink)	**: 14 dBm EIRP**
Reflection threshold	**: -70 dBm**
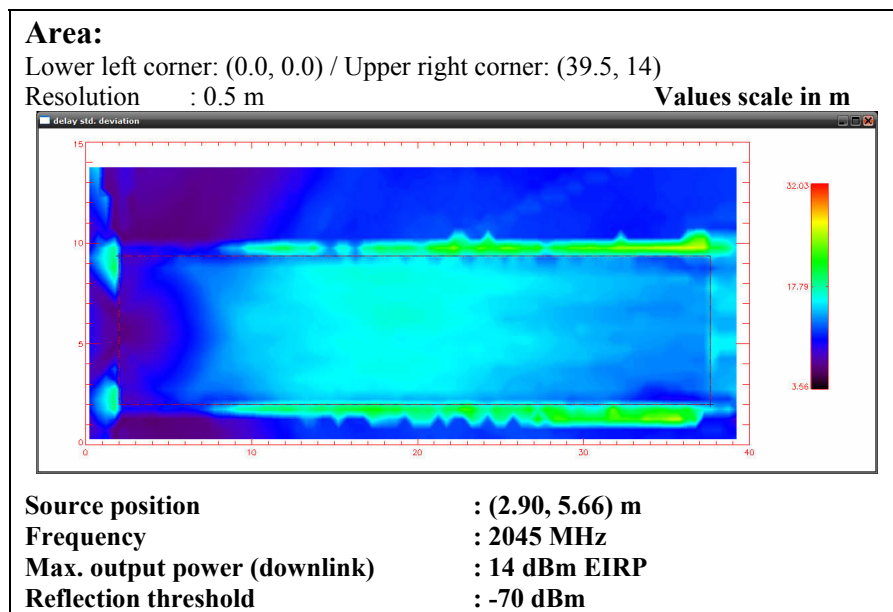
Figure 3.7 –Rms spatial delay spread, in meters.

It can be seen, as we could expect, that when a ray passes through some obstacles, especially those characterized by high permittivity values, it is produced a drastic increase of the optical path length. In the same way, where there is a zone closed by high reflective surfaces, a ray coming in generates a so high number of reflections, that the delay inside grows dramatically. This last point is well showed in the next images, where some simulations are performed in the same environment, modified with a small high-reflective rectangular structure inside (in two different positions, Figure 3.8).
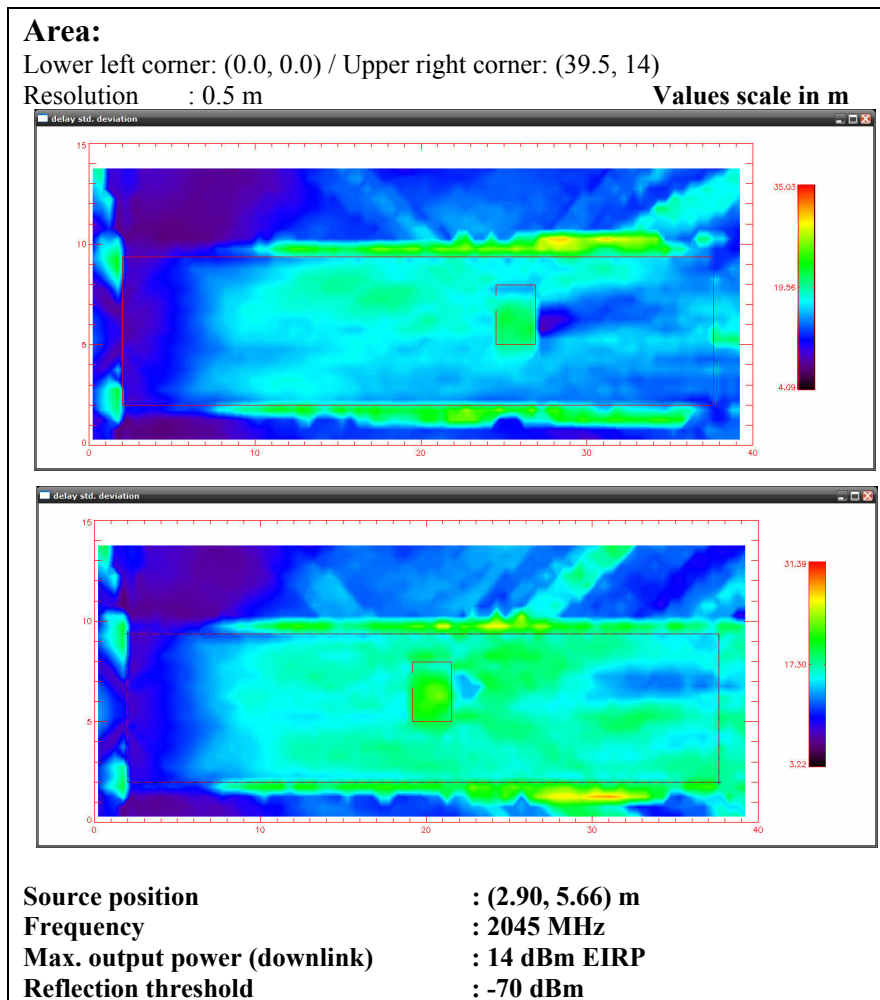
Figure 3.8 –Rms spatial delay spread, in meters.

The structure shows a small hole, through which some contributions come inside, bouncing from wall to wall and, so, increasing their delay. Obviously, the presence of the structure implies an rms delay spread increase also outside the structure, in the rest of the scene.

3.2   Simulations in realistic environments

The site chosen for a realistic simulation execution is a group of some indoors, in a warehouse located in Casoria (Naples, Italy). This site was chosen also because the building contains three rooms that were suitable to the needs, because not affected by human activities, at the moment, and devoid of furniture or objects that could affect the subsequent measurement operations. A map of the site is visible in Figure 3.9.

Downstream of an *in situ* investigation it was found that the planimetry (obtained from a paper map, using a scanner) was not sufficiently close to the actual characteristics of the environment here considered, in terms of both size and orientation of walls.
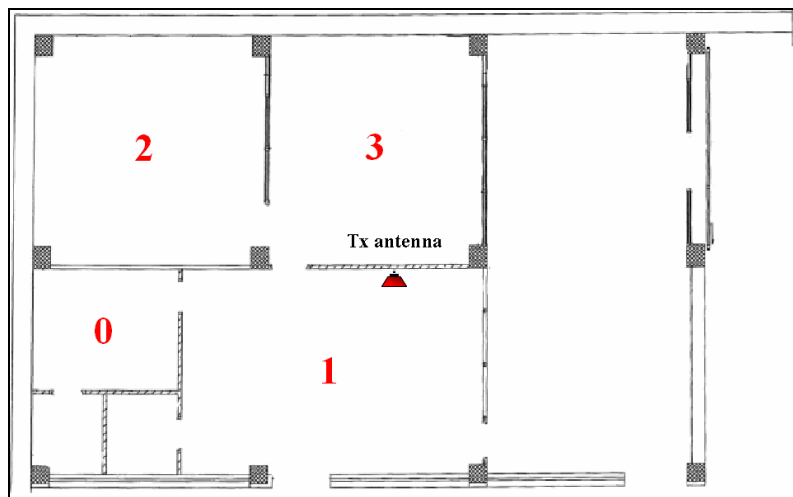
Figure 3.9 - Warehouse planimetry, acquired using a scanner.

It was necessary, therefore, to perform accurate measurements to determine the correct dimensions of rooms, the position of the various walls and their orientation. The result of these checks is visible in the image below, as it is also visible our choice for the antenna transmitter location, centrally positioned with respect to the measuring points, in order to better assess the differences between estimates and measures, in all propagation directions.
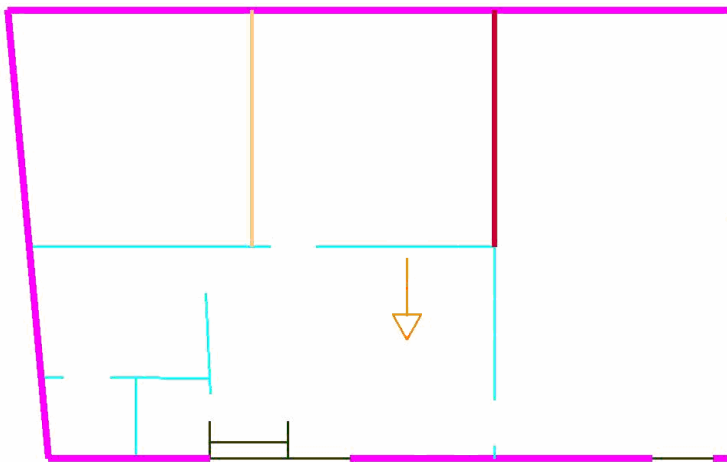
Figure 3.10 - Warehouse modified planimetry.

In order to have the data input needed by the software to work, during the map verification were examined the various components of the scene (walls, doors, etc.) to provide a list of the respective materials and thicknesses. Later it was necessary to carry out an investigation to associate material characteristics, in terms of complex permittivity, to the materials themselves.

Below there is a list of the walls composing the rooms, compiled with the same chromatic code used in Figure 3.10:

Material	ε_r	σ (S/m)	Spessore (cm.)
Type 1	5.0	0.01669	45
Type 2	2.5	0.01669	10
Type 3	2.0	0.05	3.0
Type 4	1.0	1.03E+07	10.0
Type 5	4.0	0.0005007	0.5

Table 3.1 – Warehouse walls materials characteristics.

The remaining parameters to be configured to perform simulations are:

- ❖ measured physical quantity: power to the receiver (in dBm)
- ❖ transmitted power: 14 dBm (EIRP)
- ❖ working frequency: 2045 MHz
- ❖ antenna polarization: vertical
- ❖ step (cell resolution): 0.25 metres
- ❖ reflection threshold: -55 dBm
- ❖ scene width = 19.75 metres
- ❖ scene length = 13.75 metres

The following illustrations refer to a simulation performed with the transmitting antenna in the chosen position, and related statistics.
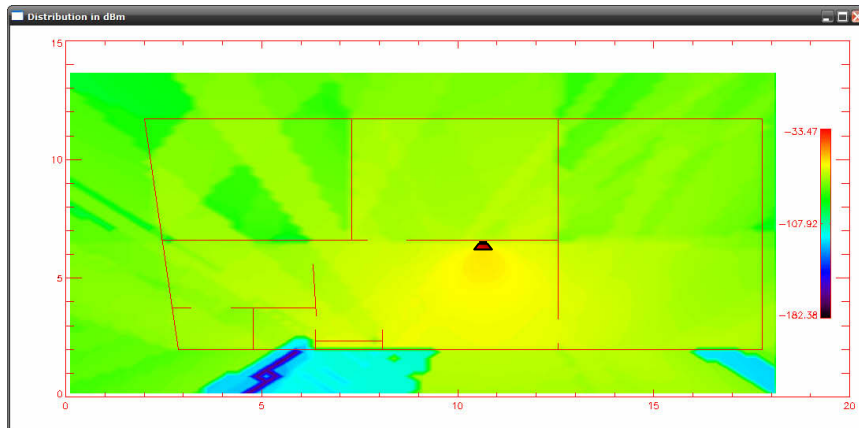
Figure 3.11 - Power distribution
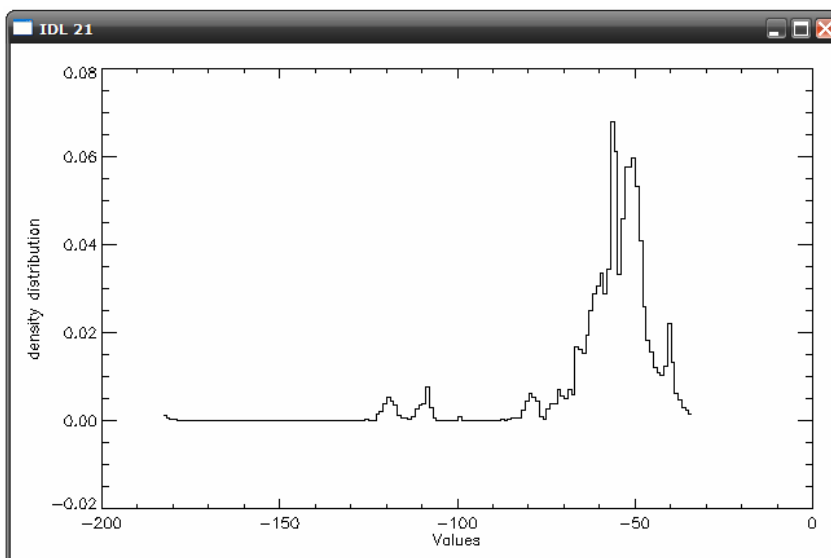
Figure 3.12 - Statistics: probability density function.
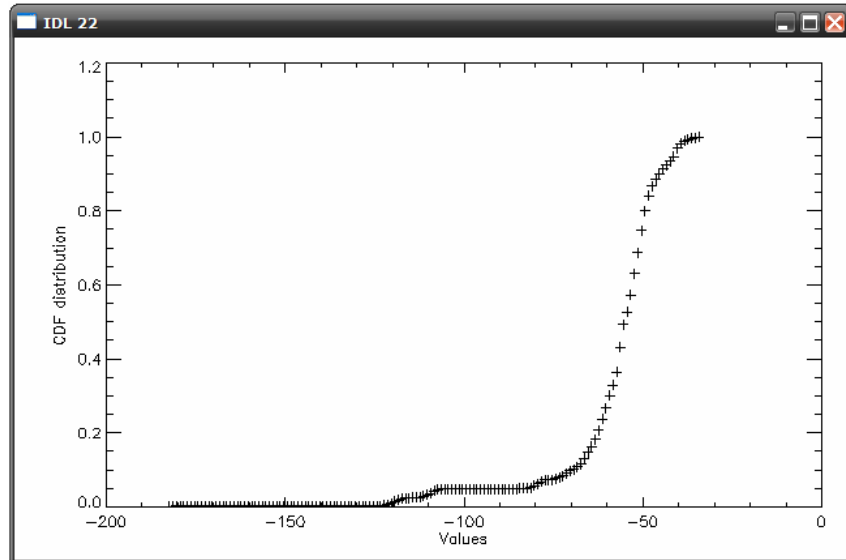
Figure 3.13 - Statistics: cumulative distribution function.

3.3   Analysis on diffraction contributions

The models here described, as said before, do not provide for diffractive contributions evaluation, when calculating total field distribution in the points of the scene involved. After algorithm completion, to justify the correctness of the choice above, was then scheduled an analysis of the consequences of neglecting diffraction phenomena. In order to do this, ad hoc changes in the code have been studied and implemented, to assess the diffraction contributions to the field distribution in canonical cases. In this section, the results of this verification are showed.

In order to take into account diffraction phenomena, which the GO, in its simplicity, makes it impossible to examine, a code integration based on GTD (Geometrical Theory of Diffraction) model can be performed. With dielectric obstacles, the formula that describes

propagation according to GTD (in a lossy medium hypothesis) is, for each contribution path j:

$$\mathrm{Pr}_j = P_T G_T G_R \left(\frac{\lambda}{4\pi r_{1j}} \right)^2 |A_j|^2 |D_j|^2 \tag{3.1}$$

where the symbols are explained here below:

$$D_j(\varphi_j, \varphi) = \begin{cases} -\dfrac{\exp[-i(\pi/4)]}{2\sqrt{2\pi k}} \left[\dfrac{1}{\cos((\varphi_j - \varphi_0)/2)} + \Gamma \dfrac{1}{\cos((\varphi_j + \varphi_0)/2)} \right] \\ \quad \text{if far from LSB/RB;} \\[2ex] \dfrac{1}{2}\sqrt{\dfrac{r_{1j}r_{2j}}{r_{1j} + r_{2j}}} \\[2ex] \quad \text{otherwise;} \end{cases} \tag{3.2}$$

$$|A_j|^2 = \frac{1}{2}\sqrt{\frac{r_{1j}}{r_{2j}(r_{1j} + r_{2j})}} \tag{3.3}$$

r_{1j} = distance from source to edge path;

r_{2j} = distance from edge to receiver path;

Γ = Fresnel coefficient for *soft* or *hard* polarization.

In Figure 3.14 the planimetry of a typical case of indoor environment, subject to diffractive phenomena, is represented. It is a rectangular room with a wall positioned inside, in order to intercept the direct field radiated from the source (represented by an asterisk at the bottom right), between the source itself and points hidden by it, hindering the spread of some rays and, probably, resulting in new contributions linked to diffraction from the upper edge.
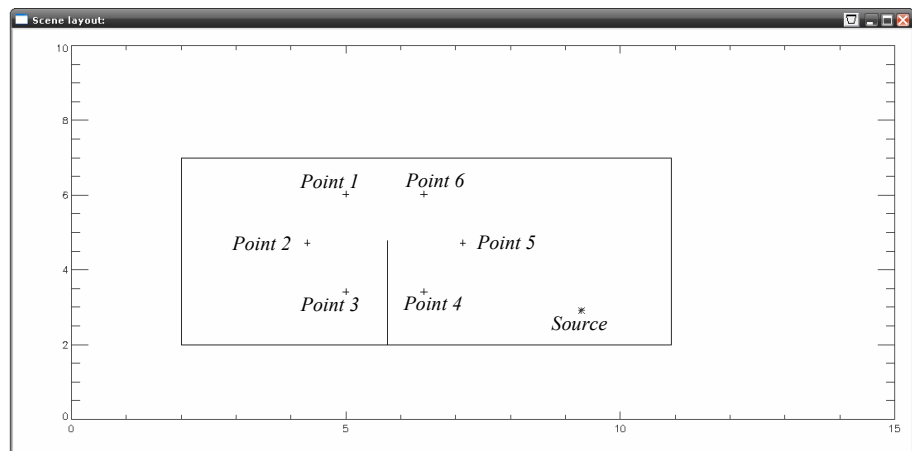
Figure 3.14 – A planimetry for diffraction analysis.

Crosses in figure, around the top of the intercepting wall, are fixed points, in which power values are assessed, in the different simulations scheduled.

The main simulation data are the following:

- environment dimensions: about 5x9 m^2;
- scene dimensions (all the field evaluation area): 9x13 m^2;
- source: omnidirectional antenna;
- radiated power (EIRP): 0.025 W;
- working frequency: 2400.00 MHz;

The perimeter walls dielectric and geometric characteristics are reported below:

- $\varepsilon_r = 10.0$;
- $\sigma = 0.005563$ S/m;
- thickness = 30.0 cm;

while the intercepting wall, in a first phase, in practise is assumed as a perfect electrical conductor.

In a first simulation (Figure 3.15) contributions reflected by perimeter walls are cancelled, to highlight the diffraction contributions of the first order over the transition zone, passing from enlightened area to shadow area (*light-shadow boundary*).
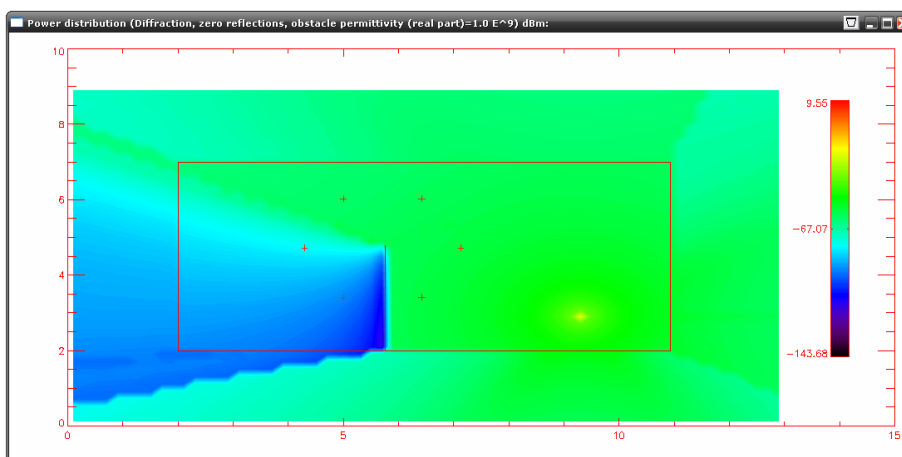
Figure 3.15 – Diffraction contributions distribution, with a metallic intercepting wall.

In this case, the omission of diffractive contributions would compromise the evaluation correctness, because of an hard discontinuity, physically senseless, of several tens of dB. It could happen easily in outdoor environments, with a weaker field confinement; in this case it is difficult to avoid relatively large error in the shadow area, without considering diffraction. In indoor environments, anyway, these problems do not longer occur, as said

before, because of an hard influence of reflections on the total field distribution.

In the following two simulations, reflections from walls are also introduced, to evaluate their effect on the total field.
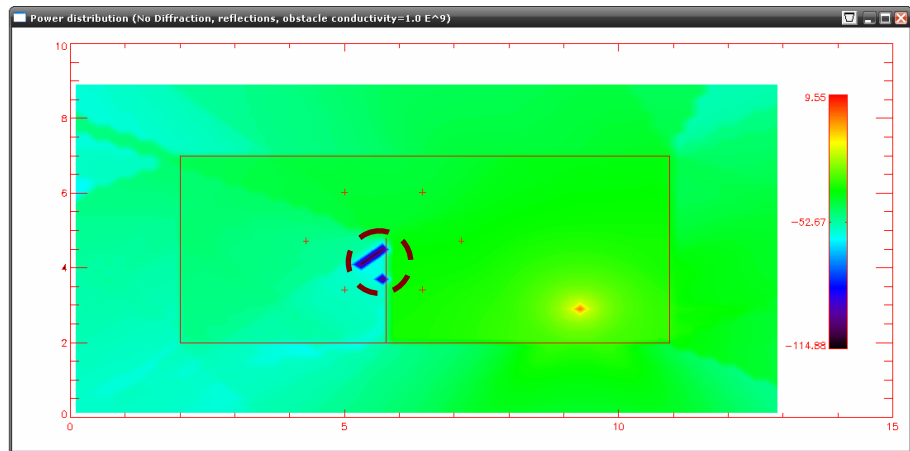
Figure 3.16 – Reflections contributions distribution, with a metallic intercepting wall.
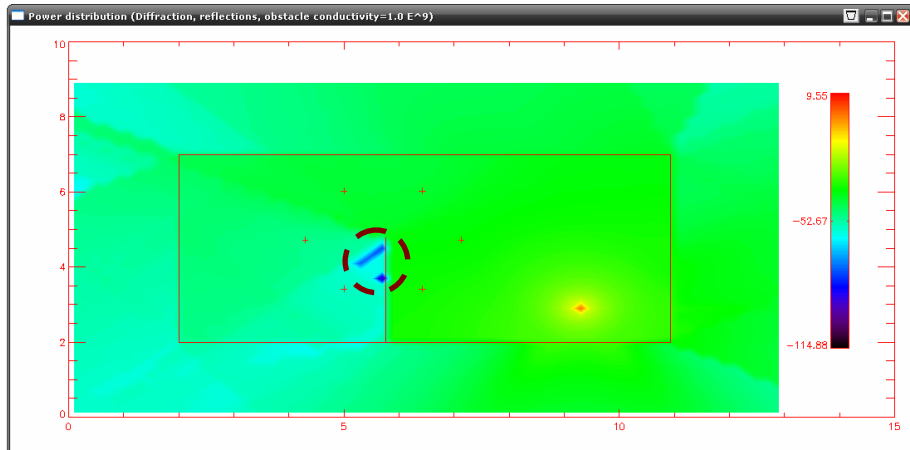
Figure 3.17 – Diffraction and reflections contributions superposition, with a metallic intercepting wall.

As showed in Figure 3.16 and in Figure 3.17, except for some few points not covered either by direct contributions and reflected ones (it only depends on both field and angular resolution), a simple visual comparison between the two images[17] practically do not underline any difference between two simulations with and without diffractions, respectively; the power difference values in the fixed points, resulting from a numerical comparison between the two matrixes, in fact, are the following:

- Difference on point 1: 0.0380 dB;
- Difference on point 2: 0.0953 dB (shadow zone);
- Difference on point 3: 0.0076 dB (shadow zone);
- Difference on point 4: 0.0001 dB;
- Difference on point 5: 0.0040 dB;
- Difference on point 6: 0.0367 dB.

The conclusion is that, in this case, the points of the scene located in the shadow area are already covered in absence of diffractive contributions, thanks to the presence of reflections by perimeter walls. The power difference values in the six points, previously selected for comparison, show that diffractive contributions are negligible, if compared to dominant ones.

This means that in an indoor environment, typically characterized by a remarkable capacity of signal confinement, neglecting diffractive phenomena (choice that would bring significant benefits, in terms of computational load) would not involve huge errors, in calculating the total field distribution on the scene.

Finally, let's analyze the same scene with an obstacle that is not a conductor (in an indoor environment, in fact, such obstacles are usually found inside the perimeter walls) but, more realistically, an inner wall with the following dielectric and geometric characteristics:

---

[17] The two simulations are here represented in false colour images using the same scale.

- $\varepsilon_r = 5.0$;
- $\sigma = 0.01669$ S/m;
- thickness = 12.0 cm;

Performing simulations with and without diffraction calculation we have the new results in Figure 3.18 and in Figure 3.19.
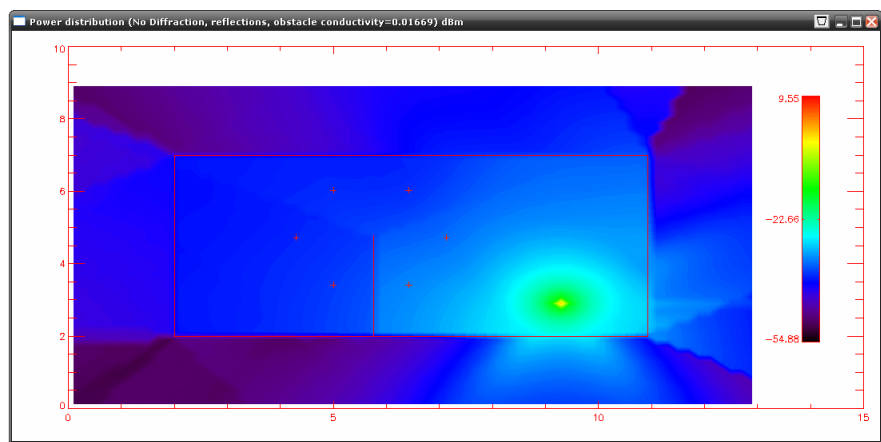

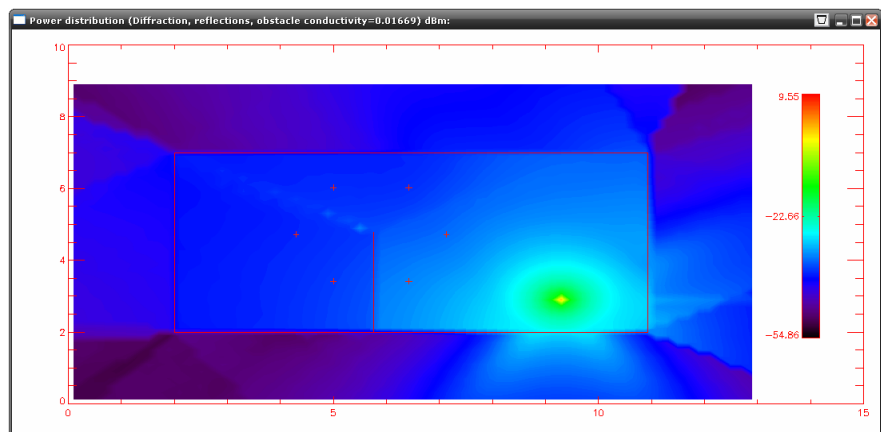**Figure 3.18 – Reflections contributions distribution, with a dielectric intercepting wall.**

Figure 3.19 – Diffraction and reflections contributions superposition, with a dielectric intercepting wall.

The values calculated on the comparison points are:

- Difference on point 1: 0.0252 dB;
- Difference on point 2: 0.0207 dB (shadow zone);
- Difference on point 3: 0.0014 dB (shadow zone);
- Difference on point 4: 0.0001 dB;
- Difference on point 5: 0.0001 dB;
- Difference on point 6: 0.0112 dB.

This proves numerically what was already obvious from a simple qualitative comparison of the two images (virtually indistinguishable). The results achieved and here presented show, as a matter of fact, that in this case (which embraces most of those possible to be considered in this type of environment) the choice to integrate in the algorithm a module for calculating contributions due to diffraction is "expensive", in terms of used resources, and almost useless, in terms of evaluation accuracy.

3.4   Measurements

Downstream the implementation of a new predictive software is necessary, of course, to go to assess how much far from physical reality are the simulation results. For this reason it was necessary to plan a measure campaign, defining an appropriate working protocol.

3.4.1 Protocol and Instruments

The chosen instruments set, entirely produced by Rhode & Schwarz, is composed as follows:

➢ R&S SMJ100A signal generator ;
➢ R&S TSMU Radio Network Analyzer;
➢ R&S ROMES Coverage Measurement System (It is the software package used for planning and executing measurement campaigns and for storing and viewing obtained values).

The receiver is equipped with a probe to measure the electromagnetic fields at the work frequencies (UMTS band). Hardware equipment for measurements includes two Centrino notebooks up to 1.8 GHz, with 1 GHz RAM, a coaxial cable connection between the transmitting antenna and the signal generator, the antenna itself, whose specifications in the UMTS band are in Table 3.2.

Frequency:	1920÷2170 MHz	Type:	Patch wall mount antenna
H-plane Beamwidth:	90°	Weight:	430 g.
V-plane Beamwidth:	60°	Gain:	7 dBi
Polarization:	E		
Dimensions:	130 mm × 260 mm x 35 mm		

Table 3.2 – Transmitting antenna characteristics.

3.4.2 Site definition

The site chosen for planned measurements execution is, of course, the same used as realistic environment for the simulations showed in chapter 3.2 (see the map in Figure 3.9).

3.4.3 Devices communication and data capture

The scheme in the figure below shows the communication links between the different devices constituting the receiving system: the TSMU device communicates with the laptop on which is installed the ROMES software by means of an IEEE 1394 (Firewire) interface, and acquires the signal through an omnidirectional antenna.
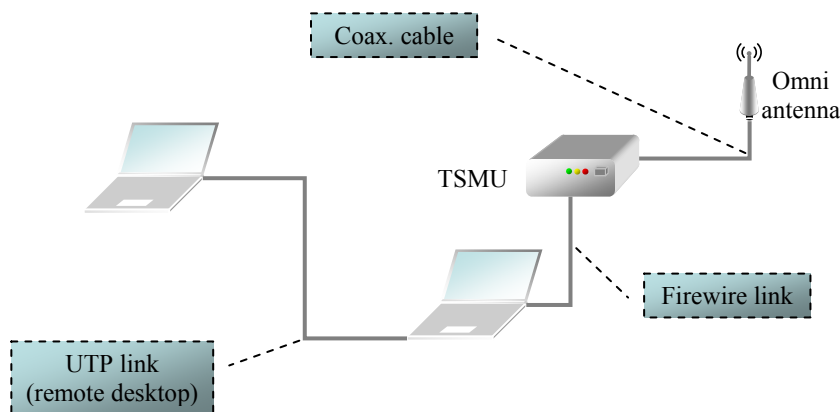
Figure 3.20 – Measuring instruments chain.

In order to minimize the possible errors on electromagnetic fields measures, due to the operator presence, the measures acquisition process is controlled remotely, using another laptop (located in room number "0", see Figure 3.9) to the first one connected in "Remote Desktop" mode, by means of an UTP cable. The rooms chosen as measurement locations were numbered from 1 to 3, as depicted in Figure 3.9, while the location for the transmitting antenna is represented, in the same figure, as a red icon. The whole receiving system was installed on a appropriate mobile platform, made of polystyrene, the receiving antenna far enough, from the rest of the equipment, to avoid (or, at least, reduce) possible (significant) measure errors, due to their proximity.

To compare, in a second step, measures with the results of software simulations that, by force of circumstances, divide the scene into

resolution cells in which the field distribution is homogeneous, it is necessary to define a similar subdivision of the real environment. First, for field level evaluation, in these cells the respective centres have to be identified (as well as for the software *cell-centres*) and then included in a measurement path defined in the planning phase, as *way-points* (measurement points).

The protocol provides for measures of power level (in dBm), to be acquired on a total number of 50 way-points, distributed in the three environments above mentioned. A map of the way-points is showed in Figure 3.21.
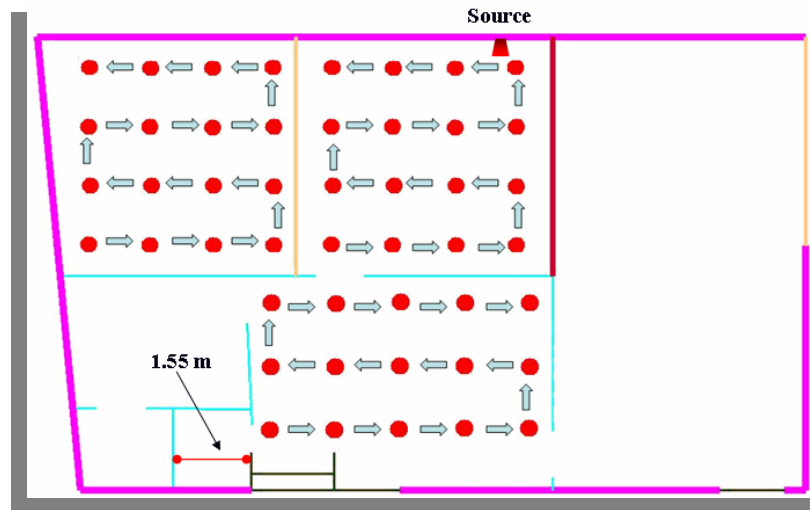
Figure 3.21 – Measurements path.

The ROMES measures management software, according to the map and to the defined way-points set, allows to trace a measurement path, like that one represented in Figure 3.21 by means of blue arrows).

The measurement protocol plans to carry out a sampling procedure in correspondence of the set points, in order to acquire (fixed the receiver height) a number of samples greater than 100 in each way-point, following the planned path.

In order to perform a comparison with the simulations results, given the models used in the simulator algorithms, it was decided to carry out multiple measurement sessions at different heights of the receiver antenna, to make a spatial average on the vertical axis; at any point, so, samples were acquired at three heights of interest: 1 meter, 1.5 meters and 2 meters from the floor. The results were, then, spatially averaged way-point by way-point.

The simulator is a tool operating essentially at the ISO-OSI stack physical level, therefore, setting aside high-level encoding and services analysis, measures were carried out in continuous wave (CW) mode, using a special receiver module. The measurements chain configuration was, therefore, the following:

* ❖ transmission/receiving mode: Continuous Wave;
* ❖ measured physical quantity: power to the receiver (dBm);
* ❖ transmitted power: 14 dBm (EIRP);
* ❖ working frequency: 2045 MHz;
* ❖ antennas polarization: vertical;
* ❖ number of samples per way-point, once fixed the receiver height: ≥ 100;
* ❖ reference height of receiving antenna: 1.0 / 1.5 / 2.0 m;
* ❖ reference height of transmitting antenna: 1.5 m.

Measurements results, once obtained for each reference height and for each room, were saved in text format files, sample by sample. These text files were, then, post-processed to provide the results to be compared with the simulations ones.

3.4.4 Measures: results and statistics

Those measures, obtained following the protocol so far developed, were acquired on the portable terminal and processed by a code for this purpose written. Data elaborations include average operations (in time and space) and uncertainty calculation.

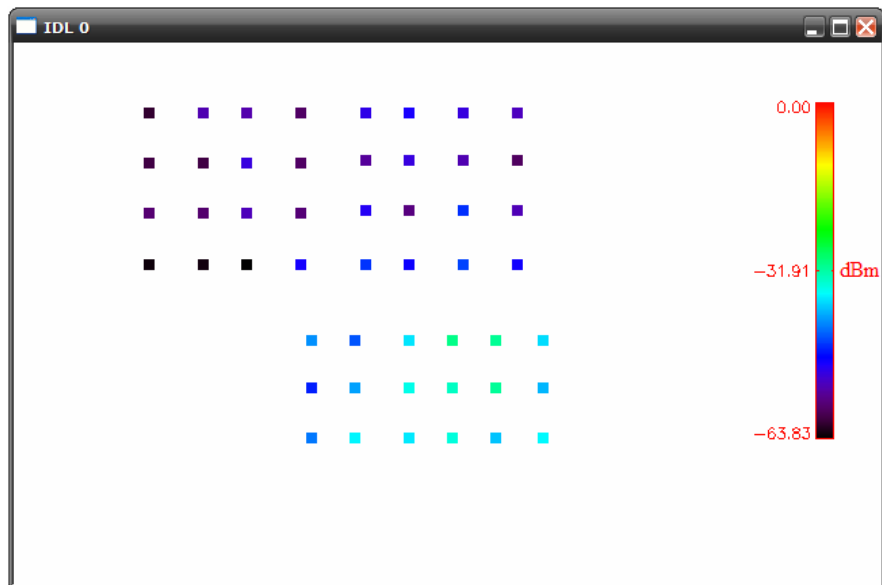The results are presented graphically in the image below.

Figure 3.22 – Measurements results in false colors.

These results are shown by means of a false colors scale on a distribution map (in matricial representation) indicating the total power average values measured on each way-point, following the path outlined before, as shown in Figure 3.21.
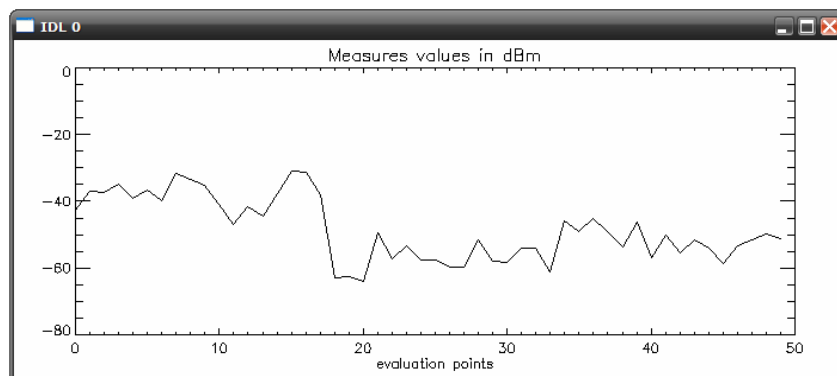

Figure 3.23 – Measurements results plot.

The same distribution, represented in 2D in Figure 3.22, can be also well represented graphically, as in Figure 3.23; the first 16 points, made by averaging in space and time all the samples taken on each way point, are those with the set of clearly highest values, refer to room 1, where it was placed the transmitting antenna.
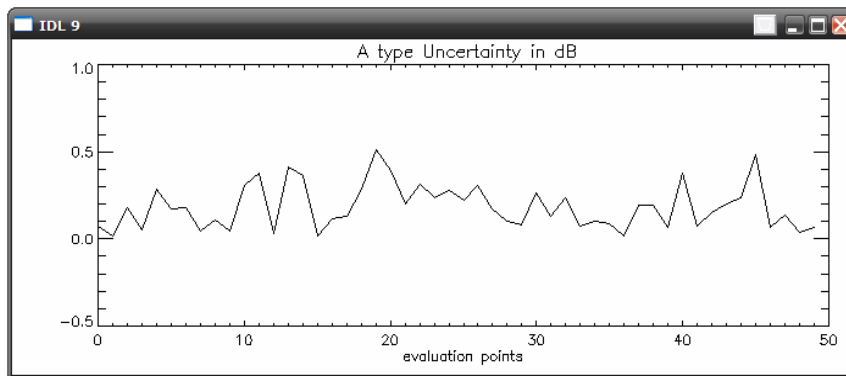
Figure 3.24 – Uncertainty: type A plot.

The "type A" uncertainty values ("type A" estimated standard deviation) are represented in Figure 3.24; they are calculated on repeated observations for each way-point.

These values must be added to the uncertainty contributions introduced by measuring instruments; an uniform distribution of possible values in a range of ± 1.0 dB around the expected value is assumed, beyond which interval the values occurrence probability is zero.

The uncertainty associated to each of the two instruments will be given, therefore, by 1/sqrt(3.0).
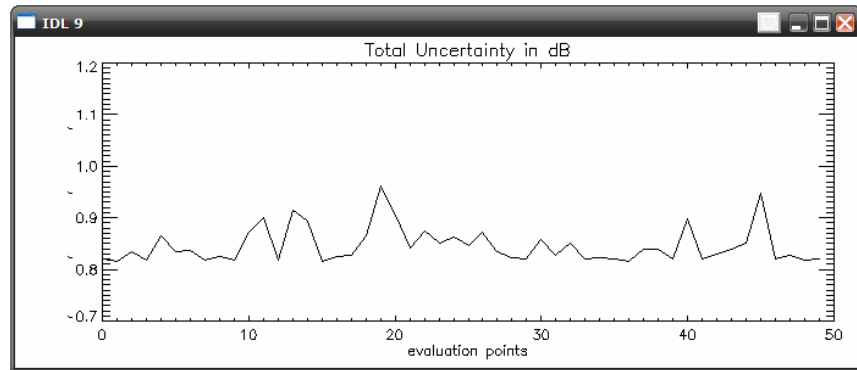
Figure 3.25 – Total uncertainty plot.

The total uncertainty, for each way-point, is shown in Figure 3.25, while in Figure 3.26 there is a graph with three curves, the central one (continue) interpolating the measures (average) values at every point, and the dashed ones representing the same values ± total uncertainty.
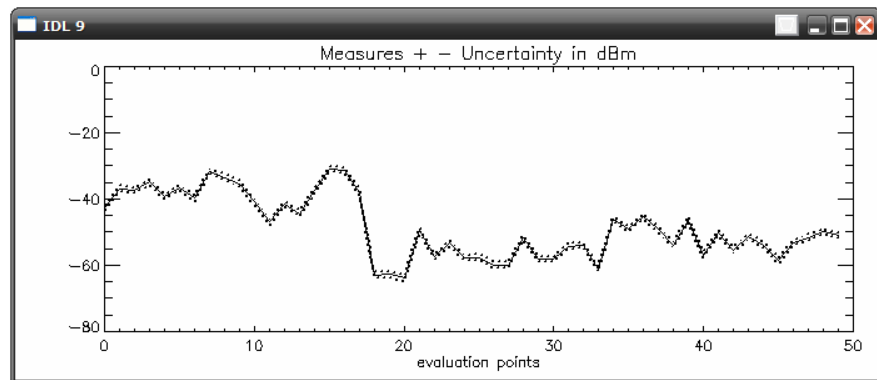

Figure 3.26 – Measures and uncertainty plots.

3.4.5 Comparison of measures and predictions

The following images graphically represent a difference between a matrix containing the measures ("MEASURES_dBm") and other matrixes, resulting from simulations in the real environment previously defined and shown in Figure 3.10 ("SIMULATION _dBm").
The matrix containing the measurement values is obtained, as before specified, making a time average (on samples corresponding to each way-point) and a space average (on the three receiving antenna reference heights).

A first comparison between measures and a simulation, with the frequency set at 2045 MHz and the transmitting antenna being positioned as in Figure 3.10, is shown in Figure 3.27.
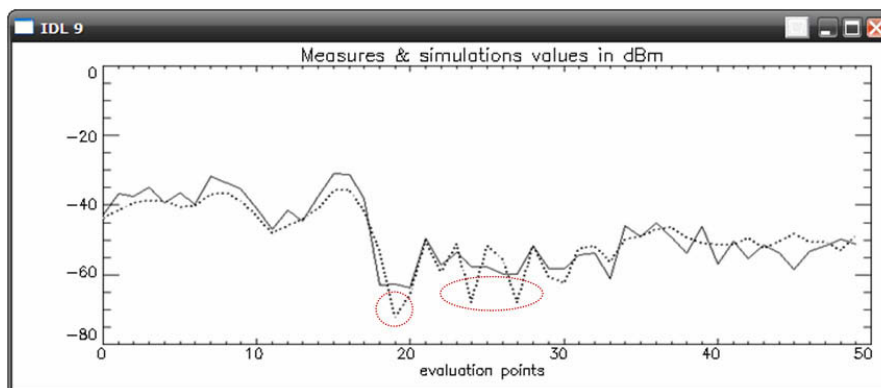
Figure 3.27 – Measures and simulation comparison, -55 dBm threshold.

The continuous curve is the measures one, while the dotted curve represents the output values from the software. In particular, the image puts in evidence three sharp fluctuations downward, in the simulation, which are not reflected in measures (between point 18 and point 28). These deviations are due to inadequate coverage of certain points in the scene, obscured by metal cabinets and, so, unreachable from the most significant reflected contributions (first order reflections).
Having neglected the diffraction phenomena, in the developed model, those points are illuminated only by very low level contributions,

associated with impinging rays coming from far, tracing long paths (with multiple obstacles interactions) and, so, rather strongly attenuated in their power content. Moreover, as we saw previously, in indoors the diffraction usually plays a minor role, compared to high order reflections (first, second, etc.) contributions.

To verify that significant contributions from secondary reflections have not been neglected, therefore, we can lower the reflection threshold. The result, shown in the chart below, in Figure 3.28 (the threshold lowered from -55 dBm to -75 dBm), is that the SIMULATION function "rebalances", now approaching better the measure plot.
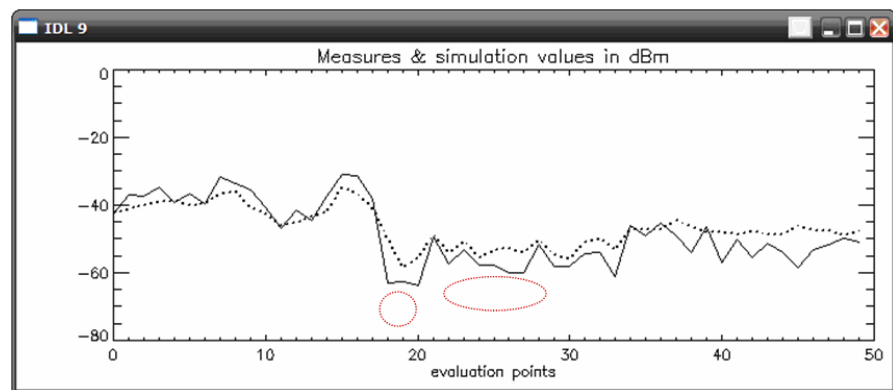
Figure 3.28 – Measures and simulation comparison, -75 dBm threshold.

Summary and conclusions

In this thesis has been discussed a model, defined to describe electromagnetic propagation phenomena, at high frequencies, in an indoor environment. The aim was to define a method useful to achieve sufficiently reliable and quick predictions of the power distribution generated, in an indoor environment, by a source located in the scene.

In order to justify the assumptions and the choices made during phenomena and environment modelization, an algorithm on these models based has been defined and, afterwards, a new software has been developed.

Thanks to this software some qualitative analyses have been made, for a first verification of the model. The simulations show a behaviour that seems coherent with theory, either in canonical and realistic environments, and confirm some choices correctness (as, for example, for diffraction contributions, here neglected).

In the software code have been also introduced appropriate functions, to add some capacity in analysis of propagation phenomena in the time domain.

To complete the models validation in quantitative terms, it was necessary to perform comparisons with measured values. For this reason a measurement campaign has been planned, finding a real environment useful to simulate and measure in the same scene, defining ad hoc protocols and choosing the necessary instruments.

The comparisons made show that simulations results are consistent with measures trend.

Acknowledgements